SANDIA REPORT

SAND2018-10703
Unlimited Release
Printed September 2018

Fundamentals of Pellet-Clad Debonding

R. Dingreville, T.J. Boyle, P.F. Weck, P.-A. Juan, S. Briggs, K.M. Hattar, D. Perales, F. Guerrero, T.H. Nguyen, X.J. Robinson, C. Barr, A. Monterrosa

Prepared by
Sandia National Laboratories
Albuquerque, New Mexico 87185 and Livermore, California 94550

Sandia National Laboratories is a multimission laboratory managed and operated by National Technology and Engineering Solutions of Sandia, LLC, a wholly owned subsidiary of Honeywell International, Inc., for the U.S. Department of Energy's National Nuclear Security Administration under contract DE-NA0003525.

Issued by Sandia National Laboratories, operated for the United States Department of Energy by National Technology and Engineering Solutions of Sandia, LLC.

Available to DOE and DOE contractors from
U.S. Department of Energy
Office of Scientific and Technical Information
P.O. Box 62
Oak Ridge, TN 37831

Telephone: (865) 576-8401
Facsimile: (865) 576-5728
E-Mail: reports@adonis.osti.gov
Online ordering: http://www.osti.gov/bridge

Available to the public from
U.S. Department of Commerce
National Technical Information Service
5285 Port Royal Rd
Springfield, VA 22161

Telephone: (800) 553-6847
Facsimile: (703) 605-6900
E-Mail: orders@ntis.fedworld.gov
Online ordering: http://www.ntis.gov/help/ordermethods.asp?loc=7-4-0#online

SAND2018-10703
Unlimited Release
Printed September 2018

Fundamentals of Pellet-Clad Debonding

Rémi Dingreville
Org. 01881
Sandia National Laboratories
Albuquerque, NM 87185-MS1315
rdingre@sandia.gov

Timothy J. Boyle
Org. 01815
Sandia National Laboratories
Albuquerque, NM 87185-MS1349
tjboyle@sandia.gov

Philippe F. Weck
Org. 08845
Sandia National Laboratories
Albuquerque, NM 87185-MS0779
pfweck@sandia.gov

Pierre-Alexandre Juan
Org. 01881
Sandia National Laboratories
Albuquerque, NM 87185-MS1315
pjuan@sandia.gov

Samuel Briggs[1]
Org. 01884
Sandia National Laboratories
Albuquerque, NM 87185-MS1056
Samuel.Briggs@oregonstate.edu

Khalid M. Hattar
Org. 01882
Sandia National Laboratories
Albuquerque, NM 87185-MS1056
khattar@sandia.gov

[1]Now at Oregon State University

Abstract

This project focused on providing a fundamental mechanistic understanding of the complex degradation mechanisms associated with Pellet/Clad Debonding (PCD) through the use of a unique suite of novel synthesis of surrogate spent nuclear fuel, in-situ nanoscale experiments on surrogate interfaces, multi-modeling, and characterization of decommissioned commercial spent fuel. The understanding of a broad class of metal/ceramic interfaces degradation studied within this project provided the technical basis related to the safety of high burn-up fuel, a problem of interest to the DOE.

Acknowledgment

This work was funded by the Laboratory Directed Research and Development (LDRD) program at Sandia National Laboratories. We gratefully acknowledge support from the Energy and Homeland Security (EHS) Investment Area (IA) committee throughout these years.

The authors would also like to acknowledge D. Perales, F. Guerrero, T.H. Nguyen, X.J. Robinson, C. Barr, A. Monterrosa.

Contents

List of Figures

Nomenclature

2D	Two-Dimensional
AM05	Armiento and Mattsson
CVZE	Cohesive Zone Volume Element
DAMAS	Design of Alloy Metals for low-mAss Structures
DFT	Density Functional Theory
DOE	Department of Energy
DPA	Displacement Per Atom
EDS	Energy Disperse X-ray Spectroscopy
EFRC	Energy Frontier Research Center
ESH	Energy and Homeland Security
FIB	Focused Ion Beam
FP	Frenkel Pair
FPA	Frenkel Pair Accumulation
FY	Fiscal Year
HAADF	High Angle Annular Dark Field
I^3TEM	In-situ Ion Irradiation TEM
IA	Investment Area
INL	Idaho National Laboratories
LAMMPS	Large-scale Atomic/Molecular Massively Parallel Simulator
LDA	Local-Density Approximation
LDRD	Laboratory Directed Research & Development
MD	Molecular Dynamics
NE	Nuclear Energy

NEUP	Nuclear Energy University Program
NP	Nanoparticles
PBE	Perdew-Burke-Ernzerhof
PCD	Pellet-Clad Debonding
PCI	Pellet-Clad Interaction
PED	Precession Enhanced Diffraction
PXRD	powder X-ray diffraction
R&D	Research & Development
RERTR	Reduced Enrichment for Research and Test Reactor
SEM	Scanning Electron Microscope
SFWST	Spent Fuel and Waste Sciences and Technologies
SNL	Sandia National Laboratories
SOLVO	Solvothermal
STEM	Scanning Transmission Electron Microscopy
TEM	Transmission Electron Microscope
UFDC	Used Fuel Disposition Campaign

1. Introduction

1.1 Scientific Challenges Related to Debonding of Complex Interfaces: A Case Study on Pellet-Clad Debonding

As of today, we are in a situation where the technical basis to assess the safety of spent nuclear fuel during long-term storage and transportation lacks meaningful data on aging effects for high burnup (defined as the fission energy release per unit mass of fuel in megawatt-days per metric ton of heavy metal of uranium (MWd/MTU), or similar units). Recent studies [15, 24] within the Department of Energy, Office of Nuclear Energy (DOE-NE) and the Research and Development (R&D) campaign formerly known as the Used Fuel Disposition Campaign (UFDC), and now named Spent Fuel and Waste Sciences and Technologies (SFWST), have revealed that the integrity of spent-fuel is highly dependent on the pellet-clad interfacial properties. One prominent spent fuel failure mechanism is due to pellet-cladding debonding (PCD), in which the fuel rod load-carrying capacity is shifted from the pellets to the cladding and the flexural rigidity of the assembly is reduced. The interface between the UO_2 ceramic fuel pellet and the Zr-based cladding materials in light water reactors (LWRs) has been shown to play an integral role in fuel integrity and performance, both during normal operation [10] and subsequent transportation and storage.[24]

Characterization of PCD relies on empirical databases that are extremely limited in terms of measurable operating conditions. The predictability of such procedures is not reliable without onerous and protracted experimental studies, since interfacial properties are dominated by microstructural and chemo-mechanical mechanisms that are not macroscopically observable. Studies available in the literature focus, for the vast majority, on pellet-clad interaction (PCI) (see e.g., [13, 17]) associated with in-reactor behavior such as fission gas induced swelling or cladding failure rather than interfacial debonding. Additionally, microstructural analyses of changes due to interfacial intermixing, elevated temperatures, and irradiation damage have been limited: characterization is either performed on a pristine surrogate material making it difficult to relate it to the true microstructural changes or aging conditions, or the microstructural analysis is done using post-irradiation optical techniques at the fuel rod scale. Such characterization clearly overlooks key grain-scale details needed to understand microstructural mechanisms associated with PCD. Although multiple national laboratories and universities are funded through the research campaigns such as the SFWST or the Nuclear Energy University Program (NEUP), microstructure characterization from real fuel rods remains challenging due to the difficulty in handling, transporting,

preparing samples, and storing highly radioactive material; not mentioning that available materials are generally on-site at nuclear power plants either in spent fuel pools or sealed in dry storage casks.

As detailed in the present SAND report and in the published manuscripts resulting from this project, research findings from this project provide a comprehensive foundation based on the mechanistic understanding of coupling effects between the interface microstructure and its chemistry on PCD properties.

1.2 Scientific Mission and Research Goals

This Laboratory Directed Research & Development (LDRD) project as a whole sought to elucidate and quantify the complex correlations and mechanisms occurring between composition, microstructure and interfacial debonding of phase boundaries, with an application to pellet-clad interface systems. This work addressed this grand challenge through a comprehensive microstructural and compositional analysis coupled with multiscale modeling and simulation. Through this approach, we attempted to answer three fundamental questions:

- **What microstructural features impact interfacial pellet-clad stability and debonding?**
  - The significant unresolved challenge here is related to our scarce understanding of the interplay between (i) simultaneous complex environments and (ii) the accumulation of defects and atomic species in materials, especially in complex interfaces.
- **What is the impact of the environment (temperature, radiation conditions, loading) on interfacial inter-mixing and interfacial debonding?**
  - The main challenge here is to develop both experimental capabilities and modeling paradigms that can integrate meaningful data in order to interrogate and probe compositional and structural changes at appropriate spatial and temporal resolutions.
- **Can we use surrogate interfaces integrated with associated computational model as a viable substitute to high burnup spent nuclear fuel system?**
  - The significant challenge here is related to availability of advanced materials synthesis techniques, experimental characterization capabilities and predictive modeling models, which, when taken together are capable of extrapolating observed and predicted on surrogate systems as a viable alternative to actual spent nuclear fuel over a broad range of environmental conditions.

This project systematically investigated this questions by:

Modeling Component Developing calibrated predictive models to simulate complex interfacial systems (surrogate and spent nuclear fuel) over a broad range of environmental conditions. Details of the technical achievements on the modeling of this project are given in Section 2.1.

Synthesis Component Synthesizing surrogate interfaces to emulate actual spent nuclear fuel interfacial materials systems in extreme environments. Details of the technical achievements on the synthesis of surrogate spent nuclear fuel are given in Section 2.2.

Microstructural Characterization Characterizing in detail the impact of microstructural features and environmental factors (thermal/irradiation) on the mechanical properties changes of pellet-clad interfaces. Details of the technical achievements on the experimental characterization of surrogate and actual spent nuclear fuel interfaces are given in Section 2.3.

Taken together, these three components have been used to determine the viability of using this integrated accelerated aging experiments and modeling method to predict performance of extended lifetime of interfacial materials systems in extreme environments (including high burnup).

2. Technical Accomplishments

2.1 Modeling the Stability and Debonding of Complex Interfaces: Multiscale Approach

In the context of experimentally characterizing and numerically modeling interfacial damage and aging processes of complex phase boundaries, the accuracy of field measurements/representations (mechanical, compositional, microstructural) are strongly linked to the quality of the interface microstructure description. This includes both the constitutive behavior of the interface and the interface constituents as well as of their morphological characteristics. Pellet-clad interfaces in commercial fuel are highly complex and separate effects from microstructure, composition, and irradiation cannot be deconvoluted.

In this LDRD project we have used a combination of various modeling and theoretical techniques in an attempt to deconvolve these aspects by studing the structure of such interfaces (Sections 2.1.1.1, 2.1.1.2 and 2.1.2.1) and the subsequent impact such interfacial structures have on debonding properties (Sections 2.1.1.2, 2.1.2.2, and 2.1.3).

2.1.1 Fundamental Thermo-mechanical Properties of (Ce,Zr)O_2/CeO_2 Interfaces: Insights from *Ab Initio* Modeling

2.1.1.1 Assessing Properties of Ceria-type Surrogates for Actinide Dioxide Nuclear Fuels

CeO_2, a surrogate for actinide dioxide nuclear fuels investigated in this LDRD project, remains challenging to study with modern computational methods based on density functional theory (DFT), owing to the strongly localized character of 4f-electron bands. Therefore, the structure-property relationships of bulk CeO_2 and Ce_2O_3 have been systematically investigated using the parameterizations of Armiento and Mattsson (AM05) and Perdew-Burke-Ernzerhof revised for solids (PBEsol) within the frameworks of DFT+U and Hubbard-corrected density functional perturbation theory (DFPT+U).

Based on elastic constants computed in this study, the dependencies of bulk, shear and Young's moduli as functions modeling assumptions have assessed within the Voigt-Reuss-Hill (VRH) ap-

proximations. Furthermore, the transverse, longitudinal and mean sound wave velocities, as well as the Debye temperature, were derived for CeO_2 and Ce_2O_3 polycrystalline aggregates and compared with experimental data. A complete analysis and discussion of our results, followed by a summary of our findings and conclusions, and details of our computational approach were reported in the following paper: **P. F. Weck, E. Kim, "Assessing Hubbard-corrected AM05+U and PBEsol+U density functionals for strongly correlated oxides CeO_2 and Ce_2O_3." Phys. Chem. Chem. Phys. 18, 26816 (2016)**.[26] For example, Fig. 2.1 shows elastic constants, transverse wave velocity (v_t), longitudinal wave velocity (v_l) and Debye temperature (θ_D) of fluorite-type CeO_2 calculated using DFPT+U with AM05, PBEsol, PBE, RPBE, PW91 and LDA functionals as a function of the $+U_{\text{eff}}$ correction for strong electron correlation.

2.1.1.2 Stability of Fluorite-Structured (Ce,Zr)O_2/CeO_2 Interfaces

While $(Ce,Zr)O_2$ bulk and nanoparticles have been the focus of active theoretical and experimental research in recent years, relatively limited information exists on the structures and fundamental thermo-mechanical properties of $(Ce,Zr)O_2$ bulk, thin films and associated interfaces with high Zr concentration.

In this LDRD project, the structures and properties of $Ce_{1-x}Zr_xO_2$ $(x = 0-1)$ solid solutions, selected $Ce_{1-x}Zr_xO_2$ surfaces and $Ce_{1-x}Zr_xO_2/CeO_2$ interfaces were computed within the framework of DFT+U.

The calculated Debye temperature increases steadily with Zr content in $(Ce,Zr)O_2$ phases, indicating a significant rise in micro-hardness from CeO_2 to ZrO_2, without appreciable loss in ductility as the interfacial stoichiometry changes. Surface energy calculations for the low-index $CeO_2(111)$ and (110) surfaces show limited sensitivity to strong $4f$-electron correlation. The fracture energy of $Ce_{1-x}Zr_xO_2(111)/CeO_2(111)$ increases markedly with Zr content, with a significant decrease in energy for thicker $Ce_{1-x}Zr_xO_2$ films. These findings suggest the **crucial role of Zr acting as a binder at the** $Ce_{1-x}Zr_xO_2/CeO_2$ **interfaces**, due to the more covalent character of Zr–O bonds compared to Ce–O. The impact of surface relaxation upon interface cracking was assessed and found to reach a maximum for $Ce_{0.25}Zr_{0.75}O_2/CeO_2$ interfaces.

To help frame the relationship between the surface properties and the interface stability, a standard model for the interfacial fracture energy, G_f, was considered. In the absence of plastic work, two indicators of the interface stability and the intensity of the interface cohesion are considered. The first indicator considers the fracture energy G_f of the $Ce_{1-x}Zr_xO_2/CeO_2$ $(x = 0.25,\ 0.50,\ 0.75,\ 1.0)$ interface slabs while ignoring the lattice relaxation of the free surfaces upon interfacial cracking (i.e. creation of free surfaces). In this case, G_f was calculated according to

$$G_f|_{\text{unrelaxed}} = \frac{1}{A}\left(E^{CeO_2}_{\text{fix-slab}} + E^{(Ce,Zr)O_2}_{\text{fix-slab}} - E_{\text{tot}}\right), \tag{2.1}$$

where A is the interface area, E_{tot} is the total energy of the interface model and $E^{CeO_2}_{\text{fix-slab}}$ and $E^{(Ce,Zr)O_2}_{\text{fix-slab}}$ are the total energies of the isolated CeO_2 and $(Ce,Zr)O_2$ slabs fixed (unrelaxed) in their respective equilibrium geometries in the interface. On the other hand, the second indicator

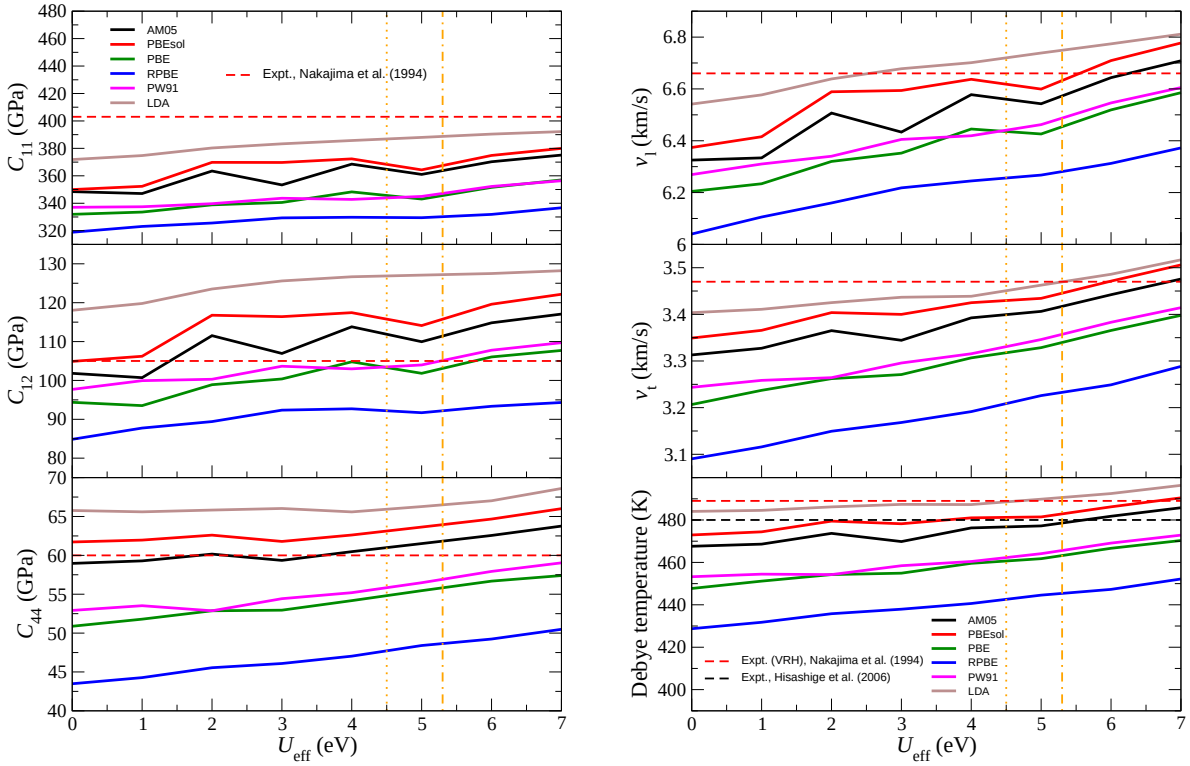

Figure 2.1. (Left) Elastic constants of fluorite-type CeO_2 calculated using DFPT+U with AM05, PBEsol, PBE, RPBE, PW91 and LDA functionals as a function of the $+U_{\mathrm{eff}}$ correction for strong electron correlation. Experimental data are indicated by horizontal dashed lines. Vertical orange dotted and dashed-dotted lines represent self-consistent linear-response $+U_{\mathrm{eff}}$ values for GGA+U and LDA+U, respectively. (Right) Transverse wave velocity (v_t), longitudinal wave velocity (v_l) and Debye temperature (θ_{D}) of fluorite-type CeO_2 polycrystalline aggregates calculated within the VRH approximation using DFT+U with AM05, PBEsol, PBE, RPBE, PW91 and LDA functionals as functions of $+U_{\mathrm{eff}}$

does account for the free surface relaxation upon interfacial cracking such that G_{f} was estimated from DFT calculations using the expression:

$$G_{\mathrm{f}}|_{\mathrm{relaxed}} = \frac{1}{A}\left(E^{\mathrm{CeO_2}}_{\mathrm{relax-slab}} + E^{\mathrm{(Ce,Zr)O_2}}_{\mathrm{relax-slab}} - E_{\mathrm{tot}}\right), \tag{2.2}$$

where $E^{\mathrm{CeO_2}}_{\mathrm{relax-slab}}$ and $E^{\mathrm{(Ce,Zr)O_2}}_{\mathrm{relax-slab}}$ are the total energies of the isolated, fully-relaxed CeO_2 and $(\mathrm{Ce,Zr})O_2$ slabs composing the interface. Note that the difference between these two indicators corresponds to the energy dissipated due to the surface relaxation upon cracking.

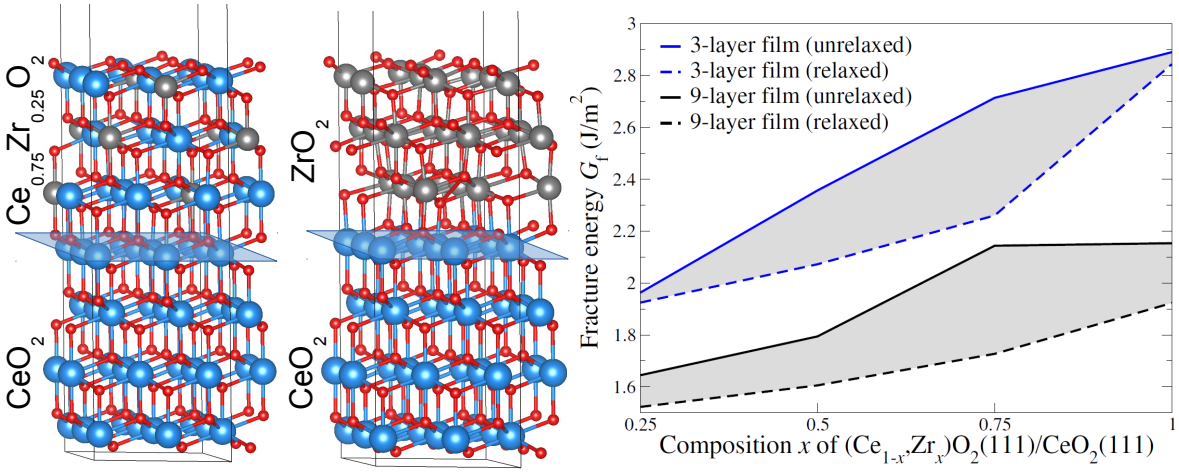

Figure 2.2. (Left) Ball-and-stick models of fluorite-structured $Ce_{1-x}Zr_xO_2(111)/CeO_2(111)$ interfaces with $x = 0.25$ and $x = 1$. Color legend: Ce, blue; Zr, grey; O, red. Blue transparent areas indicate the interface regions. (Right) $Ce_{1-x}Zr_xO_2(111)/CeO_2(111)$ fracture energy as a function of the solid solution composition $(x = 0.25 - 1)$ calculated at the GGA+U/PBE level of theory, considering the unrelaxed and relaxed states of the free surfaces upon cracking. The shaded area corresponds to the energy due to the relaxation of the free surfaces upon the creation of free surfaces during interfacial cracking. Results for 3- and 9-layer thick $Ce_{1-x}Zr_xO_2$ films are shown

An extensive analysis and discussion of our results and details of our computational approach were published in the following paper: **P. F. Weck, P. A. Juan, R. Dingreville, E. Kim, "Density Functional Analysis of Fluorite-Structured (Ce,Zr)O_2/CeO_2 Interfaces." J. Phys. Chem. C 121, 14678 (2017)**.[25] Representative models and results are represented in Fig. 2.2, which displays models of fluorite-structured $Ce_{1-x}Zr_xO_2(111)/CeO_2(111)$ interfaces and fracture energy as a function of the solid solution composition $(x = 0.25 - 1)$ calculated at the GGA+U/PBE level of theory, considering the unrelaxed and relaxed states of the free surfaces upon cracking.

In addition, variations of the interfacial fracture energy for the $ZrO_2(111)/CeO_2(111)$ interface subjected to normal compression and to in-plane expansion/compression were also calculated at the GGA+U/PBE level of theory. These results were used as input in our microstructure model and will be published in a forthcoming manuscript by **P. A. Juan, R. Dingreville, and P. F. Weck (in preparation)**. Similar models have been built and optimized for the $ZrO_2(111)/UO_2(111)$ interface and a systematic comparison with results for $ZrO_2(111)/CeO_2(111)$ is underway; results will be published in due course.

2.1.2 Structure and Debonding of U-Zr Phase Boundaries in Molecular Dynamics Simulations

2.1.2.1 Interface Dislocation Structure in Semi-Coherent Miscible Phase Boundaries: An Example for U-Zr Interfaces

As discussed in Section 2.1.1.2, properties of heterophase boundaries such as the ones found in nuclear spent fuel are partially dominated by their interfacial stoichiometry and composition. The nature of such interfaces in terms of coherency (i.e., characterized by the lattice mismatch between the two phases) is another important microstructural factor controlling their morphology and stability. As such, of particular interest to this LDRD project, the misfit dislocation networks in semi-coherent miscible phase boundaries were studied using molecular dynamics simulations in the case of U–Zr interfaces as an extreme bound of phase boundaries in spent nuclear fuel, namely cube-on-cube U–Zr interface boundaries. The main focus of this study was to shed light on the competition between chemical and elastic interactions at an (miscible) interfaces found in spent nuclear fuel.

The non-uniform dislocation structure of miscible semi-coherent bcc/bcc U–Zr interfaces was characterized using molecular dynamics simulations for various stacking orientations (namely the $\{001\}$, $\{110\}$, $\{111\}$ and $\{112\}$ boundary planes). The characterization of networks of misfit dislocations is accomplished using an atomistic computational algorithm that identifies all interfacial dislocations and their associated Burgers vectors.[21]

Discrepancies between the atomistic model and theoretical predictions pointed out the predominant role of the chemical binding over elastic interactions due to phase boundaries dislocation structures. As illustrated in Fig. 2.3 for the $\{110\}$ stacking orientation, the large gap in cohesive energies between U and Zr, combined with the miscibility of the material generated orientation dependent cohesive energy wells. For every stacking orientation studied, the large cohesive energy well overwhelmed the elastic energy features (misfit dislocation networks), rendering the interfacial excess energies near to invariant with misfit strain and therefore the subsequent debonding properties invariant with the interface structure. A complete analysis and discussion of our results, followed by a summary of our findings and conclusions, and details of our computational approach were reported in the following paper: **E.Y. Chen, R. Dingreville, and C. Deo, "Misfit dislocation networks in semi-coherent miscible phase boundaries: An example for U–Zr interfaces." Comput. Mater. Sci. 154(3), 194–203 (2018)**.[6]

2.1.2.2 Interfacial Debonding of Phase Boundaries under Irradiation Conditions in Molecular Dynamics Simulations

The atomistic simulation code LAMMPS (Large-scale Atomic/Molecular Massively Parallel Simulator [18]) is used to study the role of grain boundary structure on the phase boundary traction-separation relationship during steady-state crack growth. The simulation technique is composed of four steps: (i) creation of the grain/phase boundary, (ii) introduction of irradiation damage into

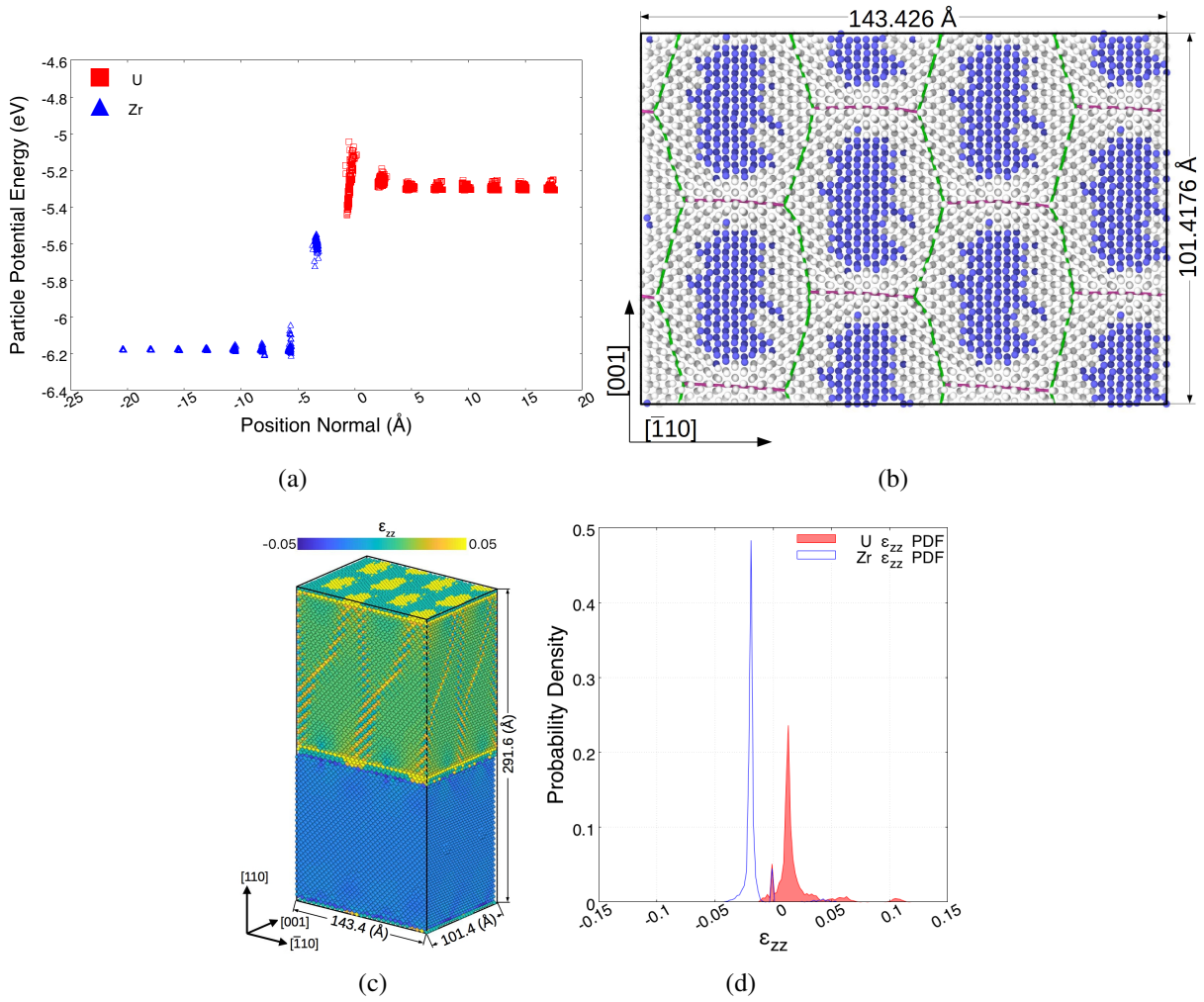

Figure 2.3. Example of (a) phase boundary energetics, (b) interface dislocation network structure (uranium atom layer adjacent to interface is shown with atoms colorized according to their respective lattice structures: blue–bcc, white–disordered), (c) normal strain field ε_{zz} and (d) probability distribution function of ε_{zz} for the $\{110\}$ stacking interfaces.The interfacial excess energy Γ is linearly correlated with the misfit strain $\varepsilon^{m,S}$. However, this dependence is weak due to the overwhelming cohesive energy well feature formed by the U and Zr atoms

the interfacial system, (iii) introduction and propagation of an atomically sharp crack, and (iv) data mining to extract the tensile strength and work of separation of the grain boundary. Most of the details pertaining to the calculation of steady-state intergranular crack propagation have been described elsewhere [1].

Grain/Phase Boundary Structure: The grain/phase boundary structure and energy are calculated using an automated approach where, for bicrystal simulation cell with three-dimensional (3D) periodic boundary conditions and a constant number of atoms, one grain is incrementally translated relative to the other, sampling a large number of initial positions, and subjected to energy minimization at each translation under stress-free boundary conditions. The translation corresponding to the minimum energy grain boundary structure after energy minimization is selected as the grain boundary structure at 0K.

Fracture Simulation: The model consists of a modeling a primary grain/phase boundary between Grain/Phase 1 and Grain/Phase 2, and absorbing layers whose purpose is to block dislocations from propagating away from the crack tip through the periodic boundary. This simulation model size selected so that the crack can propagate more than five times its initial length without significant self-image force interactions through the periodic boundaries.

After the intergranular fracture model is created, the ensemble is equilibrated to a given temperature under a hydrostatic tension using isobaric-isothermal (NPT) boundary conditions. As a result, the model is strained to provide a sufficient driving force for crack propagation (once the crack is created). Once the system is thermodynamically equilibrated, the simulation is switched to the isovolume-isothermal (NVT) ensemble, preserving the simulation cell dimensions associated with the hydrostatic prestress. Following a brief additional equilibration, an atomically sharp crack of length corresponding to the Griffith criterion is introduced in the center of the primary grain/phase boundary. The crack is created by screening the interatomic interactions between atoms in Grain/Phase 1 and Grain/Phase 2 along l_{crack} through the thickness of the model. This crack geometry does not consider crack front curvature effects. With the imposed strain due to the prestress σ_h and initial crack l_{crack}, the system is evolved for a long enough simulation time which allows both crack tips (left and right directions) to propagate along the grain/phase boundary.

The peak stress and work of separation for the grain boundary are extracted from atomic forces and displacements ahead of each crack tip by tracking the evolution of a set of cohesive zone volume elements (CZVEs) during steady-state crack propagation. Specifically, before the atomically sharp crack is introduced, each atom within a distance h on either side of the primary grain boundary is assigned to a three-dimensional rectangular volume element. The bounds of the CZVEs are determined by partitioning the prestressed system near the grain boundary into $4n$ zones with $2n$ zones above and $2n$ zones below the primary grain boundary, resulting in n CZVE pairs along the left and right crack propagation directions.

The state of each CZVE at position a X-position along the grain boundary and time t is defined by two state variables: (i) the average normal stress, $\sigma_{yy}(X,t)$, computed using the virial stress definition, and (ii) the crack tip opening displacement, $\lambda(X,t)$, computed by tracking the change in the Y-position of the center of mass of two vertically neighboring cohesive zones (normal to the grain boundary plane) as the crack propagates. Thus, each CZVE state is represented as a point (λ, σ_{yy}) at every snapshot in time. Using a statistical mechanics approach, in the limit of steady-state crack propagation that occurs over an infinitely long time over an infinitely long interface, all realized CZVE states will produce a density of states $\rho(\lambda, \sigma_{yy})$ that is a continuous function independent of time. A functional form may be fit to the data that represents the time-independent decohesion response of the grain boundary. The $\rho(\lambda, \sigma_{yy})$ data is filtered to only include data

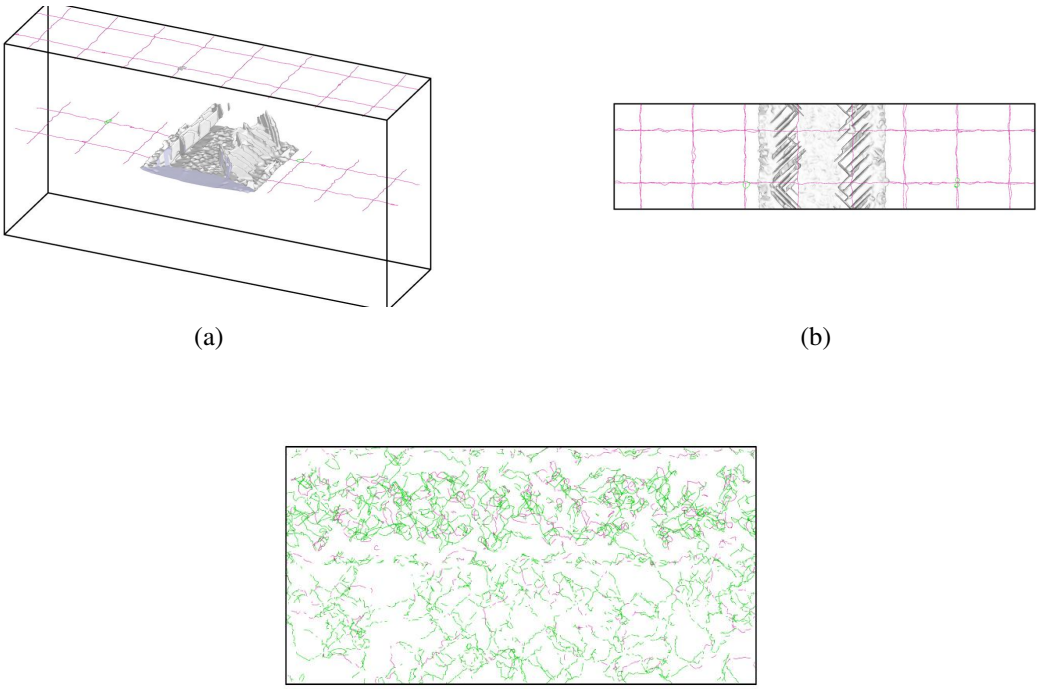

Figure 2.4. Dislocation activity during crack propagation for a pristine (i.e., no radiation damage) $\{100\}$ U–Zr interface: (a) side view, (b) top view. Interface dislocation network is colorized according to their respective lattice structures (pink) while dislocation activity resulting from crack propagation are colored using a (white) surface mesh. (c) Extended defects structure in the vicinity of the $\{100\}$ U–Zr interface at a damage level of 0.4 DPA (Displacement Per Atom). The green lines are $1/2\langle 111\rangle$ dislocation loops, the pink lines are the $\langle 100\rangle$ dislocation loops

during steady-state crack growth. Furthermore, CZVEs that are elastically deformed far ahead of the crack tip are removed from the data [1].

Radiation Damage Accumulation: During displacement cascades numerous Frenkel Pairs (FPs) with small distances between the interstitial and the vacancy are created. We used the FP accumulation (FPA) methodology [7] in order to mimic ballistic damages. This methodology circumvents the accumulation of displacement cascades by directly creating their final states, i.e., point defects. It has been proven very efficient to simulate irradiation damages in different oxides and graphite for example.[14, 16] FPA was performed using a modified version of the LAMMPS code by creating a large number of FP every 2 ps. Doing so, we impose a very high dose rate though. Damage annealing operates in these simulations by recombination of Frenkel pairs as reported in a forthcoming manuscript.

As illustrated in Fig. 2.4, this methodology has been applied to U–Zr interface systems and will be published in a forthcoming manuscript by **R. Dingreville, E.Y. Chen and C. Deo "Atomistic simulations of the debonding of U–Zr phase boundaries under irradiation conditions." to be submitted to Advanced Theory and Simulations (in preparation)**.

2.1.3 Mechanics of Finite Crack Considering Interfacial Structure: Theoretical Considerations

2.1.3.1 Mechanics of Finite Cracks in Dissimilar Anisotropic Elastic Media Considering Interfacial Elasticity

Interface structure characteristics as defined by the atomistic models described in Sections 2.1.1.2 and 2.1.2.1 have been considered in a general continuum formulation to characterize delamination and debonding phenomena in bi-material interfaces.

The basic notions of interfacial fracture mechanics have been extended to include interfacial effects such as the structural mismatch and the associated interfacial elastic response. By adopting the concept of interfacial elasticity (in the Gibbsian sense), the boundary conditions introduced are equivalent to those for a weakly bounded interfaces, i.e., the displacement jump across the interface is proportional to the traction component in terms of interfacial elastic constants. Resolution of this problem has been carried out by decomposing it into three simpler problems consisting of (i) the problem considering an uncracked bimaterial of two perfectly bonded anisotropic materials subjected to the eigenstrain, (ii) the problem of a seemingly imperfectly bonded bimaterial and subjected to known stresses at infinity and (iii) the problem of a bimaterial containing a crack lying along a perfectly bonded interface with traction forces applied on the crack faces.

One important result stemming from this formulation is that the perturbation of the elastic fields in the vicinity of the crack tip can not only be directly related to the classical difference between the elastic constants of both anisotropic solids but also to the elastic properties of the interface itself and its coupling with the bicrystal elastic constants. While the consideration of the interfacial elasticity does not affect the order of the singularity, it modifies the oscillatory effects associated with problems involving interface cracks by providing a constructive/destructive "interference" effect. This general formulation provides an insight on the physical significance and the obvious coupling between the interface structure and the associated mechanical fields in the vicinity of the crack tip. The incorporation of such interfacial properties provides a direct link between lower scale descriptions (see Sections 2.1.1 and 2.1.2) of the near-tip behavior, e.g., atomistic simulations, and their continuum description as described in this work.

A complete analysis and discussion of our formulation, and details of our theoretical approach were reported in the following paper: **P. -A. Juan and R. Dingreville, "Mechanics of finite cracks in dissimilar anisotropic elastic media considering interfacial elasticity." J. Mech. Phys. Solids, 99, 1–18 (2017)**.[11]

2.1.3.2 Defect-Interface Interactions: Elastic Green's Function in Anisotropic Bimaterials Considering Interfacial Elasticity

In addition to characterize delamination and debonding phenomena in bi-material interfaces, theoretical investigations have been conducted to investigate the interaction of defects with interfaces while considering its structure.

Within this context, the two-dimensional elastic Green's function has been calculated for a general anisotropic elastic bimaterial containing a line dislocation and a concentrated force while accounting for the interfacial structure by means of a generalized interfacial elasticity paradigm. Similarly to the problem with an interfacial crack, the introduction of the interface elasticity model gives rise to boundary conditions that are effectively equivalent to those of a weakly bounded interface. The equations of elastic equilibrium are solved by complex variable techniques and the method of analytical continuation. The solution is decomposed into the sum of the Green's function corresponding to the perfectly bonded interface and a perturbation term corresponding to the complex coupling nature between the interface structure and a line dislocation/concentrated force. Such construct can be implemented into the boundary integral equations and the boundary element method for analysis of nano-layered structures and epitaxial systems where the interface structure plays an important role.

A complete analysis and discussion of our formulation, and details of our theoretical approach were reported in the following paper: **P. -A. Juan and R. Dingreville, "Elastic Green's Function in Anisotropic Bimaterials Considering Interfacial Elasticity." J. Elast., 131, 277–296 (2018)**.[12]

2.2 Synthesis of Fluorite-Structured (Ce,Zr)O_2/CeO_2 Interfaces

2.2.1 Synthesis of Cerium Surrogates

Numerous reports indicate that cerium oxide (CeO or Ce_2O_3) would be meaningful surrogates for uranium or thorium radioactive fuels, respectively. In order to verify this, the appropriate oxides were generated in thin film and nanoparticle forms.

In this LDRD project, a variety of CeO_2 precursors were evaluated for thick film and nanoparticle production. As discussed, below, the in-house synthesized [$Ce(OR)_3$] proved to be invaluable for production of thick films. All precursors successfully produced nanoparticles of different morphologies.[4] Analysis of the nanoparticle stability indicated that upon continuous DC exposure, the particles were minimally damaged; however, rastered ion irradiation led to complete deconstruction of the nanoparticle (NP) morphology, independent of the processing route or initial morphology, while maintaining the same phase. This indicates that CeOx under certain conditions is not a useful simulant.

Molecular: A survey of the commercial Ce based compounds was undertaken to determine

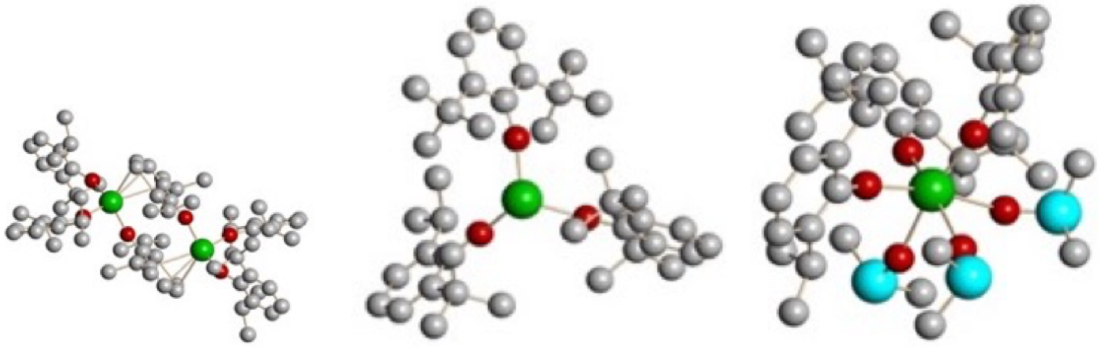

(a) (b) (c)

Figure 2.5. Structure plots of (a) [(DIP)2Ce(μ,η^6-DIP)]$_2$, (b) [Ce(DBP)$_3$] and (c) [(DIP)$_3$Ce (DMSO)$_3$]

the impact the ligand had on the final morphologies of the nanomaterials and the quality of the films generated. The precursors investigated included the halide ($CeCl_3$), acetates ($Ce(OAc)_3$), and nitrates ($Ce(NO_3)_3{\cdot}5H_2O$). In order to extend the sample size, a series of precursors were synthesized in-house, including the amide ($Ce(NR_2)_3$ where R = $SiMe_3$ (TMS)) and alkoxides ([$Ce(OR)_3$] where OR = $OC_6H_5(CH_3\text{-}2)$(oMP), $OC_6H_5(CH(CH_3)_2\text{-}2)$((oPP), $OC_6H5(C(CH_3)_3\text{-}2)$((oBP), $OC_6H_4(CH_3)_2\text{-}2,6)$((DMP), $OC_6H_4(CH(CH_3)_2)_2\text{-}2,6)$ (DIP), and $OC_6H_4(C(CH_3)_3)_2\text{-}2,6)$ (DBP). These were isolated and crystallographically characterized when possible. The two structures for the DIP and DBP compounds are shown in Fig. fig:Structure-CeO2(a) and (b). The [(DIP)$_2$Ce(μ,η^6-DIP)]$_2$ is a novel structure and full details on the structure and synthesis is presented elsewhere.[4] The [Ce(DBP)$_3$] was consistent with literature reports.[20] Additionally, some solvated complexes were isolated and an example is presented in Fig. 2.5(c) for the [(DIP)$_3$Ce (DMSO)$_3$] complex. These species were of interest due to the novelty of the precursor's arrangement or the ligand set present. A combination of the commercially available and select tailor-made precursors were used for production of the necessary nanoparticles and thin films.

Films: As part of the experimental verification of the modeling and looking for useful simulants to avoid using "hot" (radioactive) materials, a number of materials were produced as films to mimic the "hot" samples from Idaho National Laboratories (INL). All films were made by the so-called "sol-gel" approach, which involves dissolution of the precursor, followed by deposition on a support and finally thermal conversion to the oxide using ambient humidity to promote decompositions. A schematic of this process is shown in Fig 2.6. Three film sets were made (i) ceria, (ii) uranium oxide, and (iii) thorium oxide. Additional details concerning the latter two films are presented in Section 2.2.2.

Ceria Films Films of cerium oxide (or ceria) were of interest for comparison to actual sample components.[4] Details of the comparison are made elsewhere. Therefore, a series of solutions were generated by producing a 0.4 M solution of the desired precursor (commercial

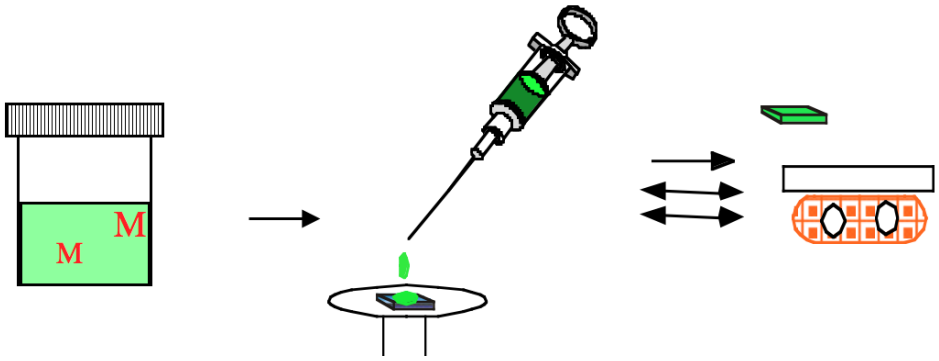

Figure 2.6. Schematic of sol-gel approach: dissolution of precursor, deposition on support, and layering by thermal conversion on a hot-plate

and select tailor-made solutions) in a solvent, and then drop casting it onto a support. These were then thermally treated to convert to the ceria phase of the material for comparison. Initial efforts focused on finding both the right precursor and exemplar support. Numerous supports were evaluated but eventually Zircaloy-4 was selected due to it being the actual component of the clad, and the best for adherence of the thick films. Commercial precursors were all found to produce very poor films, which is not unexpected based on the coordination and reactivity of the co-ligands. The alkoxides and amides Ce(NR2)3 and alkoxides [$Ce(OR)_3$], however, did prove to generate sustainable thick films. Figure WWER shows a series of films generated by the "sol-gel" method from the in-house precursors on Zircaloy-4. All samples were found to be ceria by powder X-ray diffraction (PXRD) to be ceria (CeO2; PDF 01-071-4807 or PDF01-073-7747). Eillipsometry studies were undertaken but due to the roughness of the Zircaloy support, limited the information that could be obtained on the thickness of the films. These films were sent to Prof V. Tomar (Purdue) for further analysis.

Nanoparticles: Due to the nature of the radiation destruction occurring at defect sites, it became of interest to generate nanomaterials of ceria and investigate their stability. A series of nanoparticles were produced using a solvothermal synthesis route with a wide variety of morphologies being produced. The ion beam modification and radiation stability of these nanomaterials were explored, including: nanorods from $CeCl_3$, nanocubes from $Ce(NO_3)_3$?$6H_2O$, and irregularly shaped particles from $Ce(NR2)_3$. It was found that exposure of the CeO2 to broad-beam direct-current radiation conditions did not alter the shapes of the nanoparticles; however, if a focused, rastered ion beam were used significant decomposition of the nanoparticles was observed. This indicated that rastered ion beam irradiation of nanostructured CeO2 is a poor surrogate for nuclear industry relevant radiation conditions. Figure 2.8 shows the decomposition induced by the raster ion beam on CeO_3 nanoparticles. Details of this report are being evaluated for publication and full details on this study are available elsewhere.[4]

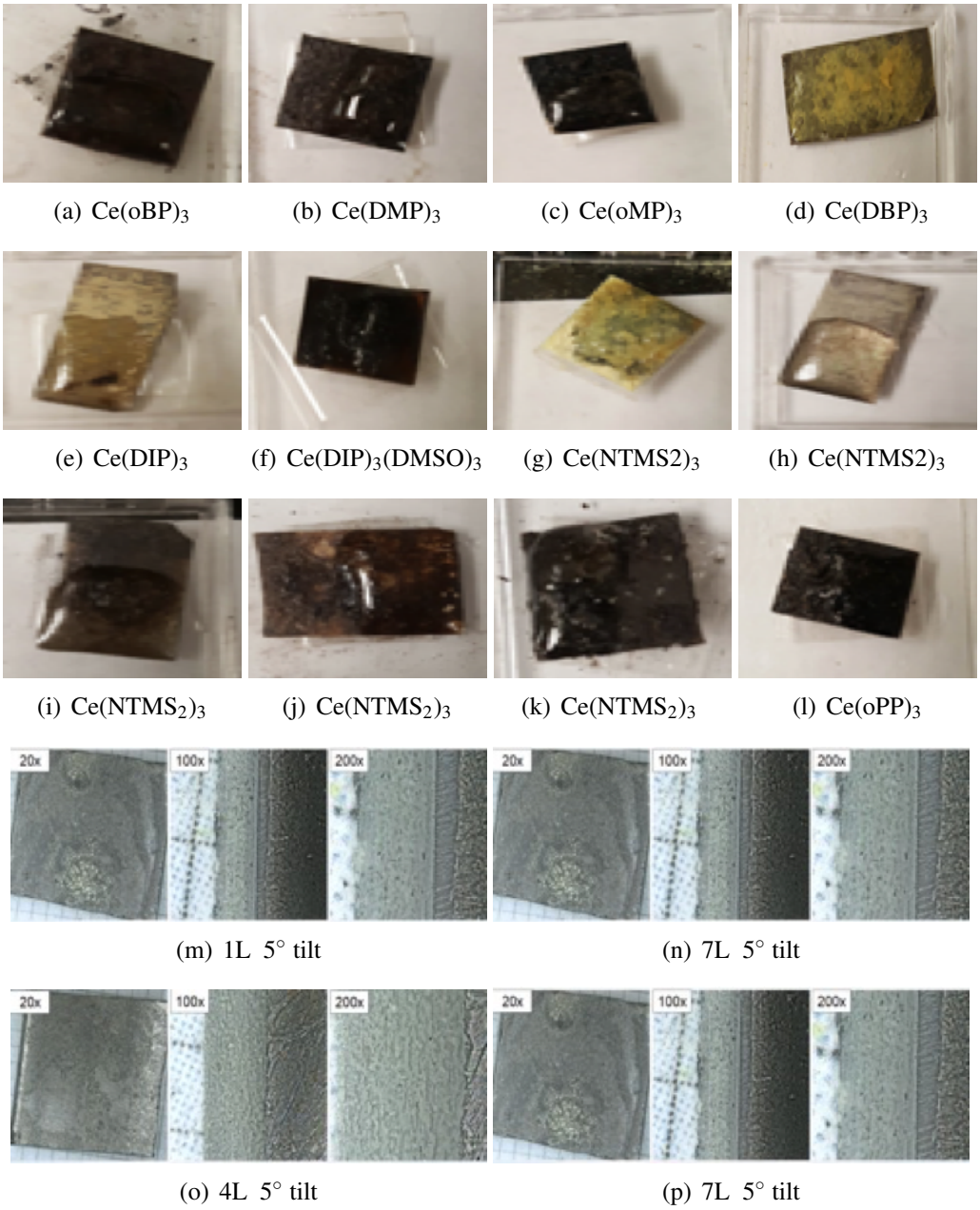

(a) $Ce(oBP)_3$ (b) $Ce(DMP)_3$ (c) $Ce(oMP)_3$ (d) $Ce(DBP)_3$

(e) $Ce(DIP)_3$ (f) $Ce(DIP)_3(DMSO)_3$ (g) $Ce(NTMS2)_3$ (h) $Ce(NTMS2)_3$

(i) $Ce(NTMS_2)_3$ (j) $Ce(NTMS_2)_3$ (k) $Ce(NTMS_2)_3$ (l) $Ce(oPP)_3$

(m) 1L 5° tilt (n) 7L 5° tilt

(o) 4L 5° tilt (p) 7L 5° tilt

Figure 2.7. Images of the [$Ce(oBP)_3$] films produced by "sol-gel" conversion and heat treatment

2.2.2 Synthesis of Actinide Materials

As the ceria surrogates proved to be less than desired stability upon exposure to a variety of ionization energies, the actual components were investigated. For these studies, derivatives of depleted uranium (d-U) and naturally occurring thorium (Th) were used for the production thin films and

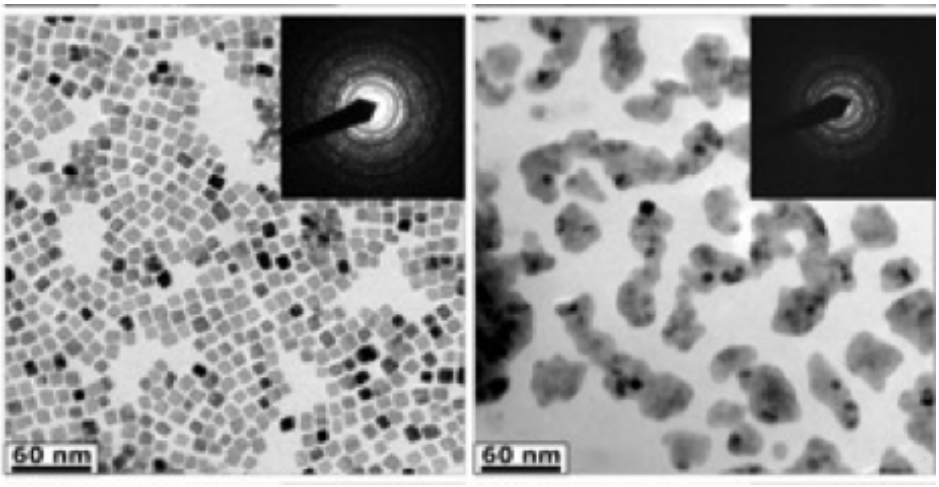

Figure 2.8. TEM images of SOLVO processed CeO_x nanoparticles for (a) pre- and (b) post-irradiation

nanomaterials. After receiving final ES&H confirmation on operations in the new Radiation Synthesis laboratory (AML 234), initial efforts focused on generating soluble uranium precursors followed by production of thick films and nanoparticle syntheses. As described below, with the new Radiation Synthesis Laboratory (AML 234) available, the d-U and Th species were investigated for thick film production. Nanoparticles were generated using solvothermal routes and commercially available precursors with a variety of morphologies and sizes available. Samples were prepared by dissolution of the acetate, chloride, and/or nitrate into a series of solvents. These solutions were drop-cast deposited onto Zircaloy supports and thermally treated to make the desired oxide phases. Due to higher than no-radiation levels, study of these films has been limited.

Molecular: All precursors were commercially available and used, upon receipt without further purification. Initial efforts focused on generating solutions of the different precursors. This was obtained by dissolution of the actinide (d-U or Th) acetate, nitrate, or chloride in a variety of organic solvents (i.e., methanol (MeOH), tetrahydrofuran (THF), pyridine (py), dimethoxy ethane (DME), iso-propanol, and dimethyl formamide (DMF)). Attempts were made to characterize these compounds with emphasis on single crystal X-ray diffraction experiments. An example of the unusual DMF/O2 structure isolated from the dissolution of $U(NO_3)_4 \cdot xH_2O$ in DMF (with heat) is shown in Fig. 2.9.

Nanoparticles: The synthesis of the actinide nanoparticles was undertaken following established routes for Ln_2O_3 nanoceramics.[4] Solvothermal (SOLVO) routes were explored for actinide oxide nanoparticles were selected due to the morphological variations available from this route. In this process, the precursors is dissolved in a solution and then added to a ParrTM bomb, sealed, and heated to decompose the precursors. A simple setup is shown in Fig. 2.10. Upon cooling, the samples were centrifuged on the benchtop, the precipitate washed with select solvents and the powders allowed to dry fully. Full details are available in the Section 2.3. PXRD analyses in-

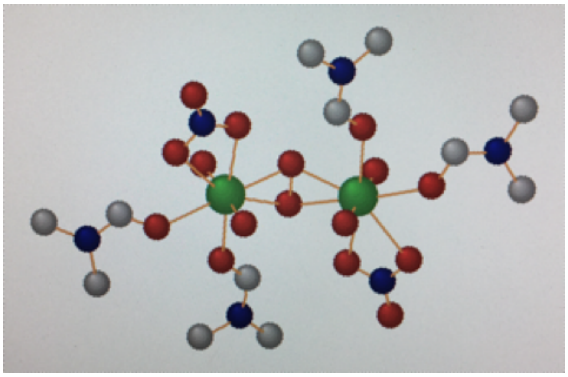

Figure 2.9. Structure plot of $[U_2O_2(NO_3)_2(DMF)_4]$

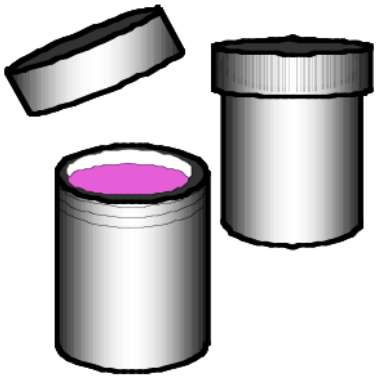

Figure 2.10. Schematic representation of a SOLVO setup)

dicated that for each sample UO_3 (PDF 00-042-1215), $UO_4{\cdot}4H_2O$ (PDF 00-016-0206), or ThO_2 (PDF 01-071-6407) were generated. Samples were slurried and drop-cast onto a TEM grid. Initial analyses indicated too few particulates had been placed on the grids or the samples were too clustered together. After sonication new samples were generated.

TEM images were collected for all samples and are shown in Fig. 2.11. The nanoparticles observed for the d-U Cl system proved to be spherical particles on the order of microns. In contrast, the d-U-NO3 appear to be irregular shaped nanomaterials mixed with hexagonal shaped nanoparticles. The irregular particles are on the order of 10-20 nm while the hexagons range from 180 to 200 nm. The ThCl4 images shown were the only images obtained and but mainly void of any material. For the Th nitrate sample, the particles appeared to be very small irregular shaped particles on the order of fractions of a nanometer. Additional work to optimize the properties of these materials are needed but the interesting shapes for the d-U samples will be

Films: Using the information garnered from the molecular complexes, attempts were made to

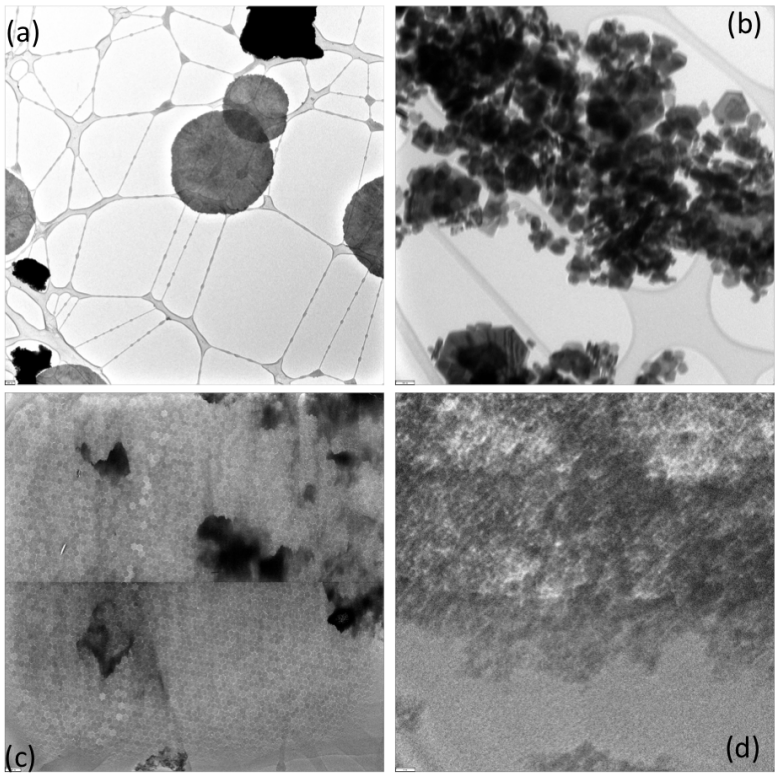

Figure 2.11. Selected TEM images of materials isolated from the SOLVO processing of (a) UCl_4 (scale bar at 200 nm), (b) $UO_2(NO_3)_2$ (scale bar at 100 nm), (c) $ThCl_4 \cdot xH_2O$ (scale bar at 100 nm) (d) $Th(NO_3)_4 \cdot xH_2O$ (scale bar at 9 nm)

generate thick films through drop-casting the actinide solution onto a Zircaloy support followed by heat treatment on a hot-plate. Specific details are discussed below.

Uranium For the d-U samples, thick films were easily produced and are shown in Fig. 2.12. The films did not fully adhere to the Zircaloy as can be noted in several of the boxes in Fig. 2.12. PXRD analyses indicated that UO_x was formed (PDF 00-031-1425, 00-036-0089) as shown in Fig. 2.13.

Thorium Additional films with the remaining Zircaloy supports were made in a similar manner, using $Th(O_2CH_3)_4 \cdot xH_2O$. Due to the limited supply of supports only two samples were generated based on the highest solubility of $Th(O_2CH_3)_4 \cdot xH_2O$ in THF and py. These are shown in Fig. 2.13. Initial PXRD analyses indicated that thorium nitride (ThN; PDF01-078-0859) may have formed (see Fig. 2.13). While it is possible that the nitride was produced, it is more likely that thorium oxide is the final product but additional analyses must be done, as the support interferes with the unequivocal identification of the materials form. There were

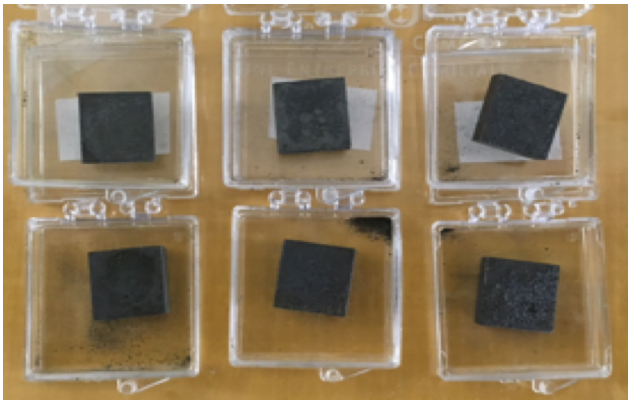

Figure 2.12. Optical images of thick films of d-UO_x films generated by dissolution of $U(OAc)_2(O)_2$ in the solvent listed

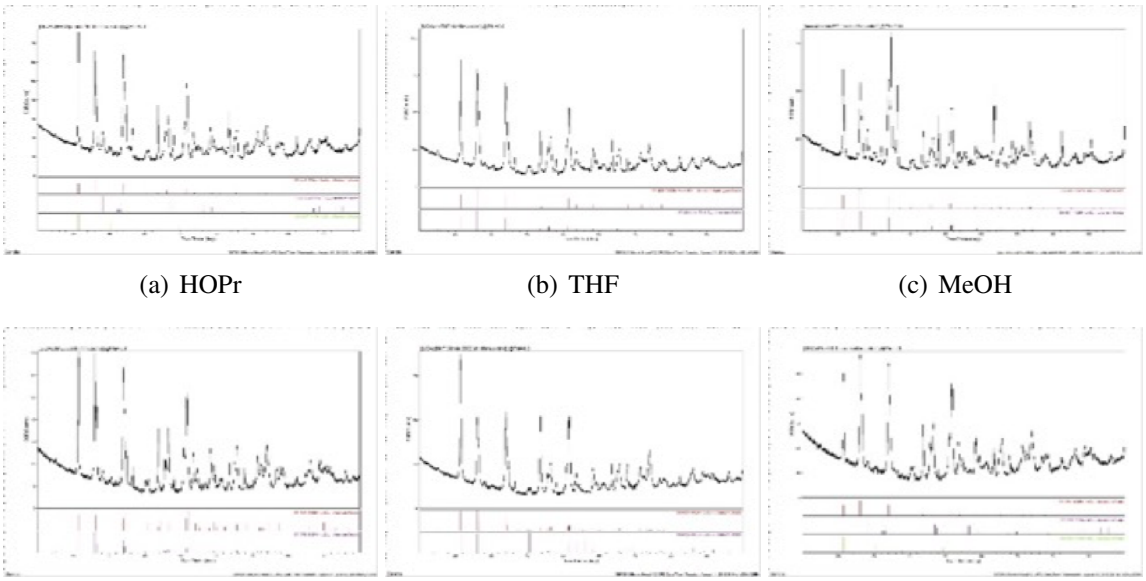

(a) HOPr (b) THF (c) MeOH

(d) DME (e) DMF (f) py

Figure 2.13. PXRD pattern of thick films of d-UO_x films generated by dissolution of $U(OAc)_2(O)_2$ in the solvent listed

substantial difficulties in analyses of these films using microscopy due to the fact that these films registered 20 dpa on a Geiger counter. This radiation due to the amount of d-U present for the entire set of samples precluded analyses on the SEM/TEM available.

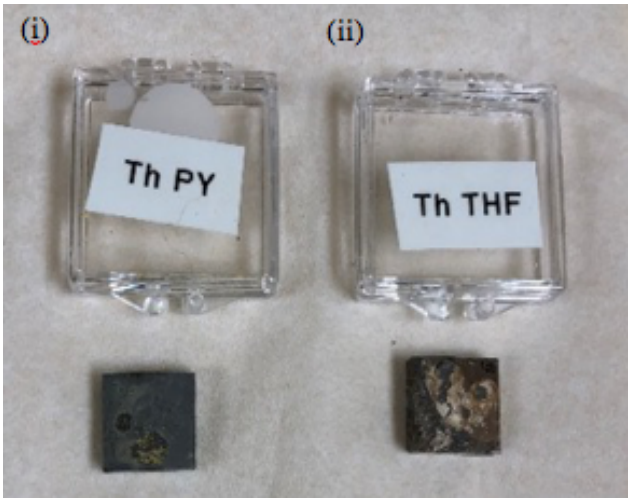

Figure 2.14. Optical images ThOx thick films from (i) py and (ii) THF

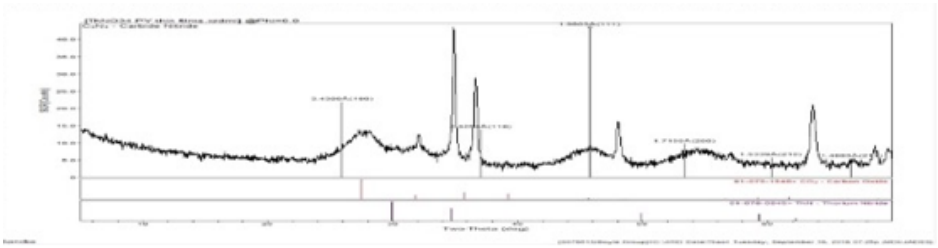

(a) py

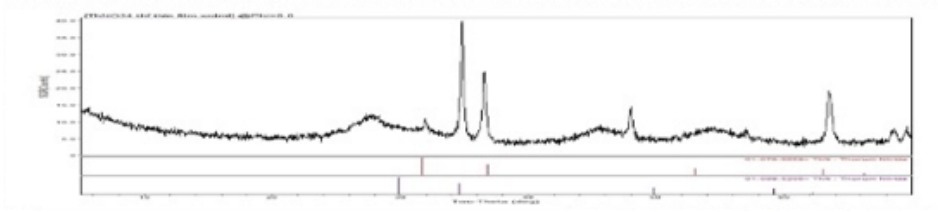

(b) THF

Figure 2.15. PXRD patterns of the ThOx thick films from (i) py and (ii) THF

2.2.3 Experimental Setup

Thin Films

Nanoparticles $An(NO_3)_4$ In a ventilated hood, $Th(NO_3)_4 \cdot xH_2O$ (0.207 g, 0.431 mmol) or $UO_2(NO_3)_2$ (0.210g, 0.532 mmol) was dissolved in 3.75 mL H_2O and added to 8.75 mL of NaOH aqueous solution in a Teflon^{TM} liner. Toluene (3.75 mL), oleic acid (0.375 mL), and dioctylamine (0.038 mL) were added without stirring and then sealed in a Parr^{TM} Digestion bomb. The mixture was heated to 180°C for twelve hours. after cooling to room temperature, the precipitate was separated by centrifugation and washed with ethanol twice. The remaining powder, white for thorium and yellow for uranium was characterized without further heat-treatment using Powder X-ray Diffraction (PXRD) and Transmission Electron Microscopy (TEM) to determine size, composition, and morphology.

$AnCl_4$ In a ventilated hood, $ThCl_4 \cdot xH_2O$ (0.511 g, 1.367 mmol) or UCl_4 (0.578 g, 1.522 mmol) was added to a mixture of 1.66 mL 5M NaOH and 11.66 mL toluene in a Teflon^{TM} liner and then sealed in a Parr^{TM} Digestion bomb. The mixture was heated to 180°C for twelve hours. After cooling to room temperature, the precipitate was separated by centrifugation and washed with H2O and EtOH two times each. The remaining powder was characterized without further heat-treatment using Powder X-ray Diffraction (PXRD) and Transmission Electron Microscopy (TEM) to determine size, composition, and morphology.

$An(O_2CCH_3C)_4$ In a ventilated hood, $Th(O_2CCH_3C)_4 \cdot xH_2O$ (0.270 g, 0.577 mmol) or $U(O_2CCH_3)_4$ was dissolved in 15 mL oleylamine in a Teflon^{TM} liner and then sealed in a Parr^{TM} Digestion bomb. The solution was heated to 180°C for twelve hours. After cooling to room temperature, the precipitate was separated by centrifugation and washed with hexanes until a fine powder remained. This remaining powder was characterized without further heat-treatment using Powder X-ray Diffraction (PXRD) and Transmission Electron Microscopy (TEM) to determine size, composition and morphology.

Powder X-ray Diffraction (PXRD) Powder X-ray diffraction (PXRD) was performed on a PANalytical X'Pert Pro diffractometer (10–100° two theta) employing Cu Kα radiation (1.5406 Å) and a RTMS X'Celerator detector at a scan rate of 3°/sec for the bulk powders or at a scan rate of 0.15°/sec using a zero background holder. The PXRD patterns were analyzed using: JADE 9 software (Materials Data, Inc., Livermore CA) and indexed using The Powder Diffraction File PDF-4+ 2013.

Transmission Electron Microscopy (TEM) TEM samples were prepared by sonicating the various nanoparticles (from $Th(NO_3)_3 \cdot xH_2O$, $ThCl_4$, and $Th(O_2CCH_3)_3 \cdot xH_2O$) for about one minute, then drop casting the dispersion onto carbon TEM grids, utilizing water as the solvent for dispersion. The samples were characterized using the JEOL 2100 TEM operated at 200 kV that is part of the In-situ Ion Irradiation TEM (I^3TEM) facility at Sandia National Laboratories.

2.3 Experimental Characterization of Complex Interfaces

2.3.1 Microstructural Characterization of Nuclear Spent Fuel

The experimental microstructural characterization conducted under this project investigated the pellet-cladding interface in a high-burnup spent nuclear fuel from two origins:

- UO_2-Zr_4 interfaces with a burnup of 72 MWd/kgU from the H. B. Robinson Nuclear Generating Station.
- U-10Mo/Zr barrier interface with moderately high burn up (4.45×10^{21} fission /cm^3) as part of the Reduced Enrichment for Research and Test Reactor (RERTR) AFIP-6MKII experiments at Idaho National Laboratory (INL), with fuel ID KGT-2144.

In both cases, specimen preparations for TEM analysis used focused ion beam (FIB) lift-out techniques. Characterization of the microstructure and microchemistry of the pellet-cladding interface used a suite of techniques including conventional TEM and high angle annular dark field (HAADF) scanning transmission electron microscopy (STEM) imaging, STEM coupled with energy dispersive X-ray spectroscopy (STEM/EDS), and precession enhanced diffraction (PED) orientation mapping.

Figures 2.16 and 2.17 illustrate the key layers identified within these interfacial systems. In both cases, the microstructural characterization showed extremely complex high-burnup structures. Interface characterization highlighted key interface features including: ultrafine grain size refinement, precipitation of solid fission products, formation of intermetallic rich region and formation of a nanocrystalline porous.

Details reporting these finding will be published elsewhere.

2.3.2 Radiation Stability of Morphologically Varied Cerium Oxide Nanoparticles

As detailed in Section 2.2.1, this work sought to explore the response of CeO_2 nanoparticles to ionizing radiation.

A series of morphologically varied CeO_2 NP were generated from commercial [chloride ($CeCl_3$), nitrate hydrate ($Ce(NO_3)_3{\cdot}6H_3O$)] and in-house synthesized amide [($Ce(NR_2)_3$ where R = ($Si(CH_3)_3$) and alkoxide [2,6-di-tert-butyl phenoxide ([$Ce(DBP)_3$]), 2,6-di-iso-propyl phenoxide ([$(DIP)_2Ce(\eta^6$-DIP)]$_2$, neo-pentoxide ([$Ce(ONep)_3]_4$)] precursors. As illustrated in Fig. 2.18, the morphologies of subsequent CeO_2 NP were identified by PXRD and TEM as: nanorods ($CeCl_3$), nanocubes ($Ce(NO_3)_3{\cdot}6H_2O$), and irregularly shaped [$Ce(NR_2)_3$; post processed at 800 °C; and ([$Ce(DBP)_3$], [$(DIP)_2Ce(\eta^6$-DIP)]$_2$, [$Ce(ONep)_3]_4$)].

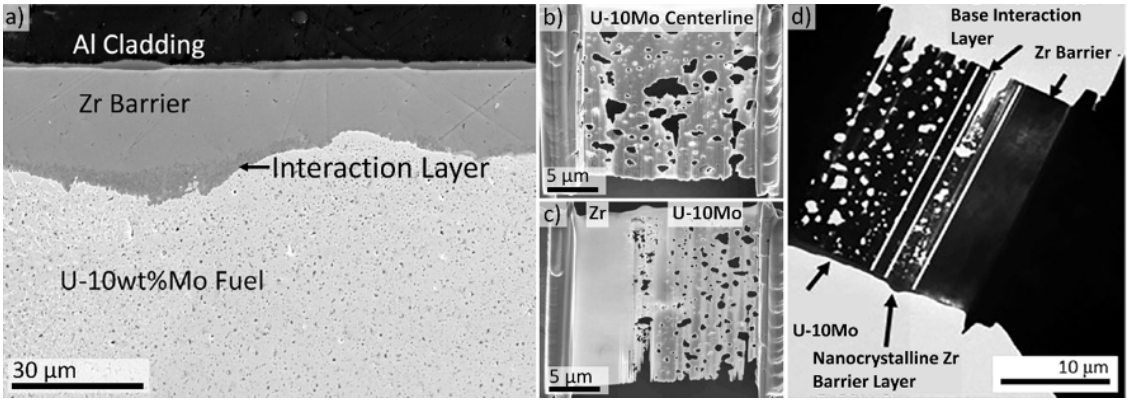

Figure 2.16. a) overview of the U-10Mo fuel plate with key layers identified; b) SEM image of the U-10Mo fuel center line cross-sectional TEM liftout; c) SEM image of the U-10Mo/Zr interface layer cross-sectional TEM liftout; d) low magnification TEM image of the U-10Mo/Zr interface liftout with key layers identified including U-10Mo fuel, base interaction layer, nanocrystalline Zr barrier layer, coarse grain Zr barrier layer

Exposure of the CeO_2 to broad-beam direct-current radiation conditions yielded no impact on the morphology for each sample investigated; however, exposure to a focused, rastered ion beam of identical ion energy, species and fluence resulted in significant decomposition of the nanoparticles. The results of these studies imply that the details concerning the radiation conditions are critically important in determining the stability of nanostructured materials. However, this effort suggests that rastered ion beam irradiation of nanostructured CeO_2 is a poor surrogate for nuclear industry relevant radiation conditions, but has potential for tailoring the nanostructure morphology and the subsequent properties.

2.3.3 Stability of Hafnia Nanoparticles Coated by a Silica Shell (HfO_2/SiO_2)

As part of our investigation into radiation damage, this program investigated an unusually stable material, hafnia nanoparticles coated by a silica shell (HfO_2/SiO_2). This study found that the HfO_2/SiO_2 core/shell nanoparticles could withstand extensive bombardment from both high energy heavy ions and low energy light ions.[2] In addition, these core/shell nanoparticles are stable to thermal annealing up to 800 °C. This indicates that the core/shell structures may enhance nanoparticle radiation stability and may be a useful piece of information concerning pellet clad storage. Additional experimental and modeling efforts are needed to fully understand the impact this unusual behavior might have on radiological storage. As illustrated in Fig 2.19, this work reveals that core/shell structures contribute to increased radiation tolerance in nanoparticles due to their ability to prevent sputtering and either store displacement defects and implanted He or allow

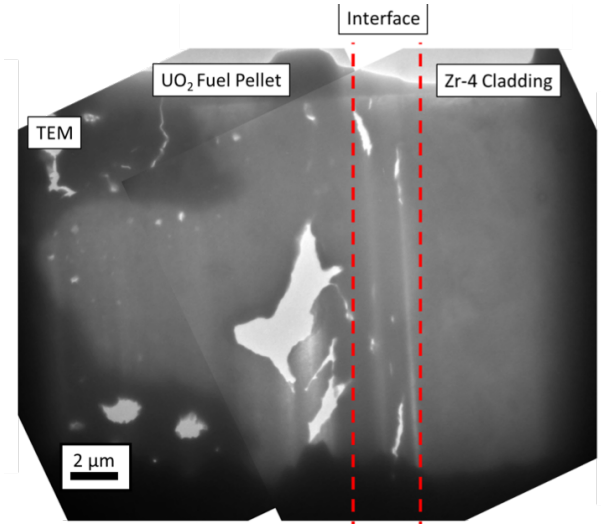

(a)

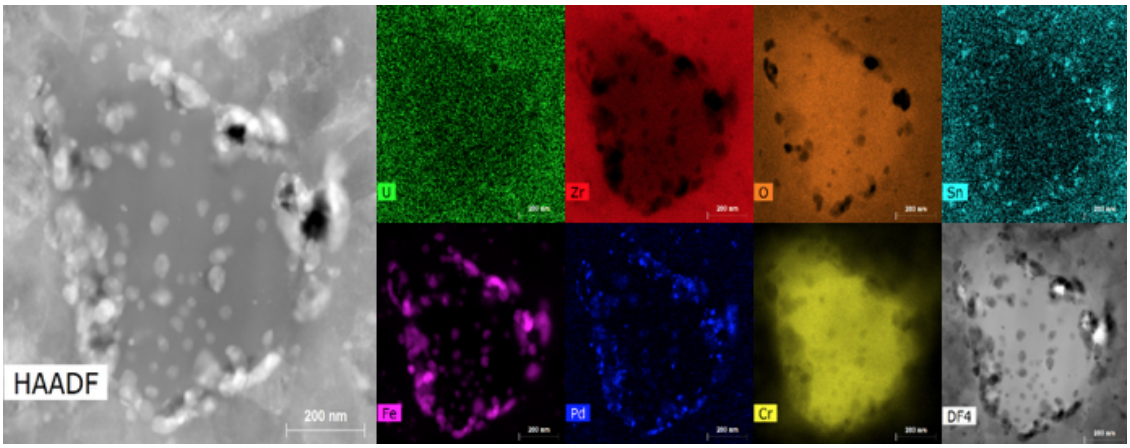

(b)

Figure 2.17. a) overview of the H.B. Robinson specimen with key layers identified; b) STEM-EDS of the precipitation of solid fission products in the vicinity of the interface

them to diffuse out of the core/shell structure. Ultimately, the apparent resistance of this HfO_2/SiO_2 core/shell structure to damage in extreme irradiation and thermal environments, as well as the proven functionality of HfO_2 in radiation therapy dose enhancement suggest that the core/shell structure may show promise for future cancer therapy concepts and micro-electronics design for radiation environments. Future work to understand the underlying mechanisms that contribute to the radiation damage resistance and the second shell formation noted for these core/shell nanoparticles is critical to exploiting the interesting properties noted here. This work has been published elsewhere.[2]

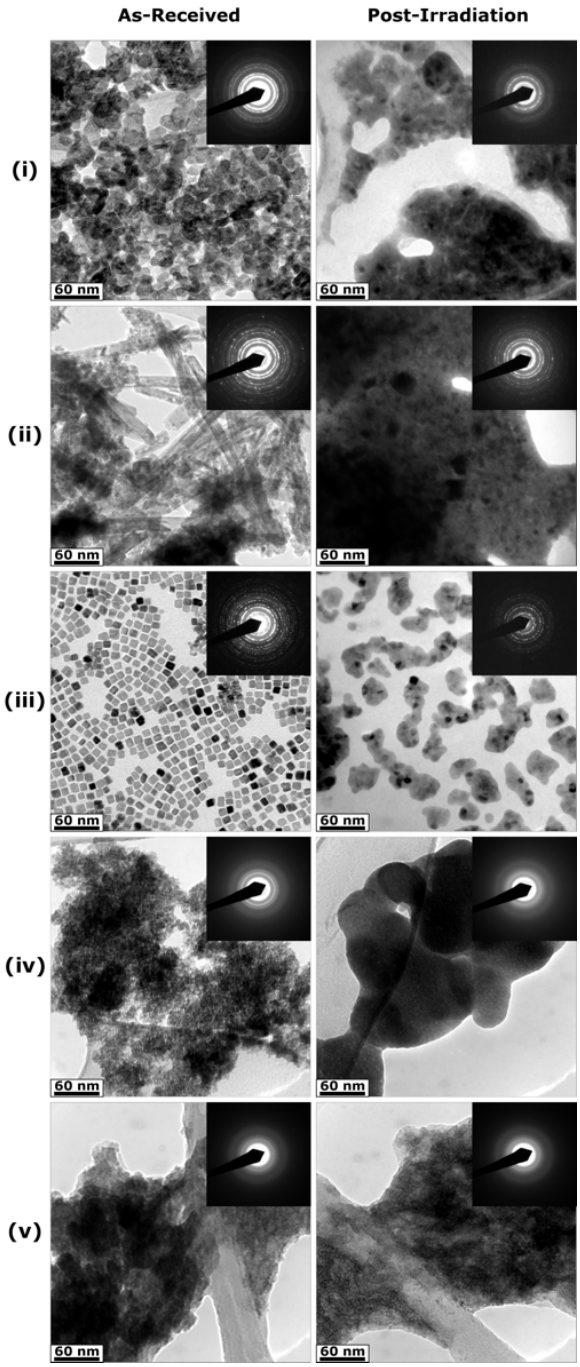

Figure 2.18. TEM images of SOLVO processed materials pre- and post-exposure to rastered high level irradiation: (i) 1-Cl, (ii) 2-Cl, (iii) 1-NO_3, (iv) 1-NR_2, (v) 1-DIP

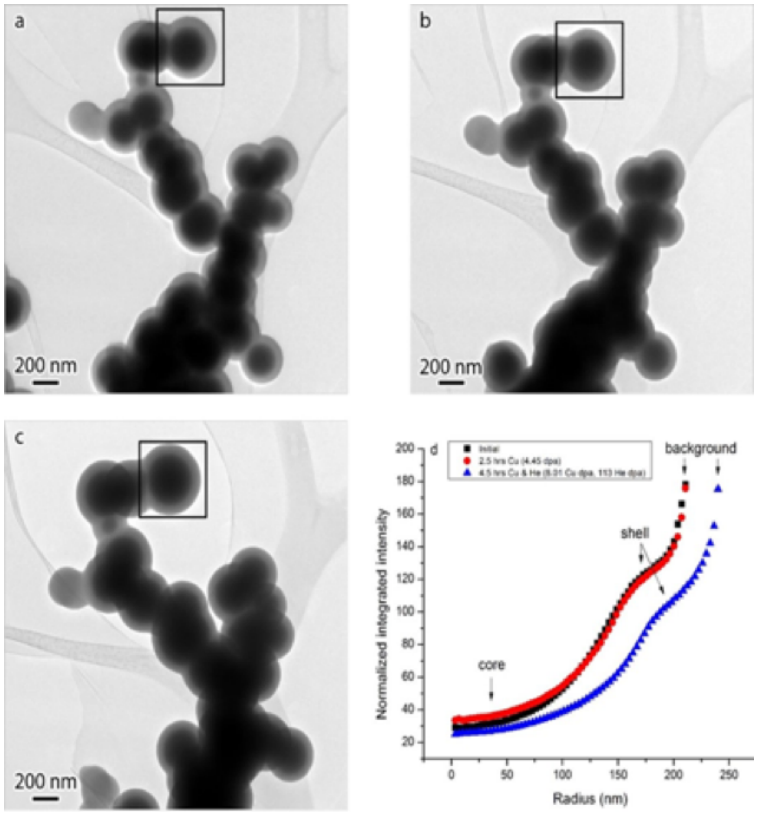

Figure 2.19. In-situ TEM images of HfO_2/SiO_2 core/shell nanoparticles (a) pre-, (b) 2.5 h of Cu irradiation, and (c) g 4.5 h of simultaneous irradiation

3. Project Legacy

3.1 Publications

At the time of drafting this SAND report, this work resulted in the publication of fourteen manuscripts in peer-reviewed journals. To this date, these include:

1. Zarnas, P. et al., "Mechanics of point defect diffusion near dislocations and grain boundaries: A chemomechanical framework." **Computational Materials Science**, 144, pp. 99-112, 2018. [27]

2. Spearot, D. E. et al., "Atomistic Simulation Techniques to Model Hydrogen Segregation and Hydrogen Embrittlement in Metallic Materials." **Handbook of Mechanics of Materials**, pp.1-34, 2018. [19]

3. C. Sun, et al. "Formation of tetragonal gas bubble superlattice in bulk molybdenum under helium ion implantation." **Scripta Mater.**, 149, pp. 26-30, 2018. [22]

4. Dennett, C.A. et al., "Detecting self-ion irradiation-induced void swelling in pure copper using transient grating spectroscopy." **Acta Mater.**, 145, pp. 496–503, 2018. [8]

5. T.J. Boyle, et. al. "Synthesis and Characterization of Tris(trimethylsilyl)siloxide Derivatives of Early Transition Metal Alkoxides that Thermally Convert to Varied Ceramic-Silica Architectures." **Inorganic Chem.**, 57(15), pp. 8806–8820, 2018. [3]

6. Blair, S. J. et al., "Unexpected radiation resistance of core/shell ceramic oxide nanoparticles." **Mater. Today Comm.**, 2018. [2]

7. Chen, E.Y. et al., "Misfit dislocation networks in semi-coherent miscible phase boundaries: An example for U–Zr interfaces." **Comput. Mater. Sci.**, 154, pp. 194–203, 2018. [6]

8. Taylor, C.A. et al., "In situ TEM multi-beam ion irradiation as a technique for elucidating synergistic radiation effects." **Mater.**, 10(10), pp. 1148, 2017. [23]

9. Bufford, D.C. et al., "Cavity formation in Molybdenum studied in situ in TEM." **Fusion Sci. Technol.**, 71(3), pp. 268–274, 2017. [5]

10. Juan, P.-A. and Dingreville, R., "Elastic Green's Function in Anisotropic Bimaterials Considering Interfacial Elasticity." **J. Elast.**, 31(2), pp. 277–296, 2018. [12]

11. Juan, P.-A. and Dingreville, R., "Mechanics of finite cracks in dissimilar anisotropic elastic media considering interfacial elasticity." **J. Mech. Phys. Solids**, 99, pp. 1–18, 2017. [11]

12. Weck, P.F., et al., "Density Functional Analysis of Fluorite-Structured (Ce,Zr)O_2/CeO_2 Interfaces." **J. Phys. Chem. C**, 121(27), pp. 14678–14687, 2017. [25]

13. Dingreville, R. et al., "A primer on selecting grain boundary sets for comparison of interfacial fracture properties in molecular dynamics simulations" **Scientific Reports**, 7(1) pp. 8332, 2017. [9]

14. Weck, P. F. and Kim, E., "Assessing Hubbard-Corrected AM05+U and PBEsol+U Density Functionals for Strongly Correlated Oxides CeO_2 and Ce_2O_3." **Phys. Chem. Chem. Phys.**, 18(38), pp. 26816–26826, 2016. [26]

3.2 Presentations and Outreach to the Scientific Community

At the time of drafting this SAND report, this work resulted in twenty two presentations at technical conferences domestically and internationally, with twelve of those being invited presentations. Additionally, twelve invited technical seminars have been given at universities and research institutes. To this date, these include:

List of contributed and invited ($\star$) presentations

1. *R. Dingreville "Examples and challenges of multiscale predictive simulations of microstructures in harsh environments." Joint Sandia-Georgia Tech Materials Workshop, December 2015; Atlanta, GA.

2. *D.C Bufford et al., "Correlating grain orientation and grain boundary character to the failure path in nanocrystalline metals." International Symposium on Plasticity and Its Current Applications; January 2016; Kona, HI.

3. *K. Hattar "Investigating overlapping and harsh environments via in-situ TEM." International Symposium on Plasticity and Its Current Applications; January 2016; Kona, HI.

4. *K. Hattar "In situ TEM Investigations of Overlapping and Harsh Environments." 2nd Joint Sandia-Georgia Tech Materials Workshop; February 2016; Albuquerque, NM.

5. R. Dingreville et al. "On the interaction of solutes with GBs: A disclination-based model." TMS 2016 Annual Meeting & Exhibition, March 2016; Nashville, TN.

6. K. Hattar, et al., "Recent advancements in Sandia's In situ Ion Irradiation Transmission Electron Microscope." The Fourth Workshop On TEM With In Situ Irradiation, March 2016; Orsay & Gif sur Yvette, France.

7. *K. Hattar, "In situ Ion Irradiation Transmission Electron Microscope at Sandia National Laboratories." Nuclear Science User Facilities Ion Beam Investment Options Workshop; March 2016; Idaho Fall, ID.

8. P.-A. Juan et al., "Mechanics of finite crack considering interfacial elasticity." 24th International Congress of Theoretical and Applied Mechanics (ICTAM), August 2016; Montreal, QC, Canada.

9. D. Perales, et al. "Film study of pellet-clad interactions using cerium oxide as a surrogate." Rio Grande Symposium, October 2016; Albuquerque, NM.

10. R. Dingreville et al. "Structure of semi-coherent U-Zr (miscible) interfaces." TMS 2017 Annual Meeting & Exhibition, March 2017; San Diego, CA.

11. *K. Hattar and D. Hanson, "Sandia's Experimental Radiation Capabilities." NSUF facility meeting, May 2017; Idaho Fall, ID.

12. *R. Dingreville and P.-A. Juan "Mechanics of finite crack considering interfacial elasticity." SIAM Annual Meeting (AN17), July 2017; Pittsburgh, PA.

13. R. Dingreville et al. "A primer on selecting grain boundary sets for comparison of interfacial fracture properties in MD simulations." 2017 LAMMPS Workshop & Symposium, August 2017, Albuquerque, NM.

14. P.-A. Juan et al., "Characterization of fracture and fragmentation phenomena across multiple length scales: from atomistic to macroscopic approaches." MS&T17 Materials Science & Technology Conference & Exhibition, October 2017; Pittsburgh, PA.

15. S.A. Briggs, et al. "Synthesis and characterization of d-UO2 nanoparticles for nuclear fuel microanalysis." Fall MRS; November 2017, Boston, MA.

16. *R. Dingreville, "Mechanics of (finite) interfacial cracks." International Conference on Plasticity, Damage & Fracture (keynote), January 2018, San Juan, PR.

17. *R. Dingreville, "Mechanics of (finite) interfacial cracks." German and European Physical Societies, Spring Meeting, March 2018, Berlin Germany.

18. P.-A. Juan et al., "Competition of deformation modes in irradiated Zr alloys: a micromechanical approach." TMS 2018 Annual Meeting & Exhibition, March 2018; Phoenix, AZ.

19. D. Perales, et al. "Evaluating pellet-clad interactions using cerium oxide simulants and depleted thorium and uranium oxide thin films on zircaloy." 255th National Meeting and Exposition of the American-Chemical-Society (ACS) - Nexus of Food, Energy, and Water, March 2018; New Orleans, LA.

20. *S.A. Briggs et al. "Exploring factors affecting radiation response in nanoparticles." WOTWISI-5, April 2018; University of Huddersfield, UK.

21. *C.M. Barr, et al. "Exploring the interplay between grain boundaries and radiation damage." 25th International Conference on the Application of Accelerators in Research and Industry (CAARI 2018), August 2018; Gaylord Texan Resort in Grapevine, Texas.

22. *P.-A. Juan et al., "Competition of deformation modes in irradiated Zr alloys: a micromechanical approach." Microstructure & Property Relationship of Polycrystalline Materials: Characterization and Modelling workshop, September 2018; Santa Fe, NM, USA.

List of invited technical seminars

1. R. Dingreville, "Hydrogen Effects in Microstructures: The Camel's Nose Analogy." Center 6200 Technical Seminar Series, November 2015; Albuquerque, NM.

2. K. Hattar, "In situ Ion Irradiation Transmission Electron Microscope at Sandia National Laboratories." French Atomic Energy Commission (CEA) September 2016; Orsay/Saclay, France.

3. R. Dingreville, "On the interaction of hydrogen with grain boundaries." Mechanical Engineering Technical seminar, October 2016; Boulder, CO.

4. K. Hattar, "Exploring the Response of Materials to Radiation with In-situ Microscopy." University of New Mexico, Graduate Student Seminar, September 2016; Albuquerque, NM.

5. K. Hattar, "Correlating Mechanisms and Properties in Extreme Environments Utilizing Advanced Electron Microscopy." Department of Mechanical Engineering Seminar at University of Texas, El Paso March 2017; El Paso, TX.

6. K. Hattar & R. Dingreville, "Nanomaterials Response to Radiation Environments." Department of Nuclear Engineering Graduate Student Seminar, University of New Mexico, April 2017; Albuquerque, NM.

7. K. Hattar, "Understanding and Tailoring Nanomaterials for Extreme Environments." University of Florida, Nuclear Engineering Seminar, August 2017; Gainesville, FL.

8. K. Hattar, et al. "Nuclear Science User facility Program: Sandia Participation and Opportunities." Department of Nuclear Engineering Graduate Student Seminar, University of New Mexico, November 2017; Albuquerque, NM.

9. K. Hattar, "Exploring Materials in Extreme Environments with Nanometer Resolution." University of Florida, Materials Science & Engineering Seminar, November 2017; Gainesville, FL.

10. K. Hattar, "Deconvoluting Reactor Environmental Effects with Nanometer Resolution." University of California, Berkeley, Nuclear Engineering Department Seminar, January 2018; Berkeley, CA.

11. K. Hattar, "Understanding and tailoring nanomaterials for extreme environments." Los Alamos National Laboratories, March 2018; Los Alamos, NM.

12. K. Hattar. "Exploring extreme environments with nanometer resolution." UC, Riverside MSE Seminar, May 2018; Riverside, CA.

3.3 Intellectual Property

At the time of drafting this SAND report, this work resulted in two US patent application:

1. Boyle, T. J.; Chan, R. O.; Sears, J. M.; Hernandez-Sanchez, B. A. "**Single-source synthesis of ceramic oxide nanoparticles**" with the Patent Application #20180179112. The present invention relates to ceramic nanoparticles and, in particular, to the single-source synthesis of ceramic oxide nanoparticles, including core/shell ceramic oxide nanoparticles.

2. Provisional patent filed Boyle, T. J.; Chan, R. O.; Sears, J. M.; Hernandez-Sanchez, B. A. "**Metal-siloxide precursors for the single-source synthesis of ceramic-silica nanomaterials**" with provisional patent #SD13725/S142427.

Further details on the inventions can be found by using the Patent Application #.

3.4 Proposals Submitted and Awarded

At the time of drafting this SAND report, this work resulted the drafting and submission of five research proposals, with two of them awarded funding for future work building on the technical achievements resulting from this work. These include:

1. LDRD: "Multi-Resolution Characterization of the Coupling Effects of Molten Salts, High Temperature and Irradiation on Intergranular Fracture." R. Dingreville as Principal Investigator. Awarded FY19-FY21.

2. LDRD: "Developing Microstructure-Property Correlation of Radiation-Tolerant Nanoporous and Nanostructured Materials for High Irradiation Environments." R. Dingreville as Principal Investigator. Awarded FY17-FY19.

3. Energy Frontier Research Center (EFRC). Selected for full proposal. "Energy Frontier Research Center for Materials Discovery for Combined Extremes (MaDeX)." R. Dingreville as Principal Investigator. FY18. Not funded.

4. Nuclear Energy University Program (NEUP): "A Multiscale Chemomechanical Framework for Corrosion and Irradiation Degradation of Structural Alloys in Molten Salt Reactor Environment." Prof. J. Qu, Tufts University, as Principal Investigator. FY17. Not funded.

5. NEUP: "Deciphering irradiation-induced thermal aging mechanisms of cast austenitic stainless steel through multiscale experimental characterization." Prof. L. Capolungo, Georgia Institute of Technology as Principal Investigator. FY17. Not funded.

3.5 Awards, Professional Leadership & Recognition

At the time of drafting this SAND report, this work resulted one award and professional leadership recognition.

1. R. Dingreville was awarded an international visiting scholar fellowship at Center for National Scientific Research (CNRS) to work at the Laboratory of Excellence "DAMAS" (Design of Alloy Metals for low-mAss Structures). R. Dingreville was hosted by prof. S. Berbenni to work on a novel general theory of two-way chemo-mechanical coupling of interfaces. Details about LabEx DAMAS can be found on its website: `www.labex-damas.com`.

4. Summary and Conclusions

As described in the Sections above, this LDRD project sought to systematically elucidate and quantify the complex correlations and mechanisms occurring between composition, microstructure and interfacial debonding of phase boundaries, with an application to pellet-clad interfacial systems through the use of a unique suite of novel synthesis of surrogate spent nuclear fuel, in-situ nanoscale experiments on surrogate interfaces, multi-modeling, and characterization of decommissioned commercial spent fuel. The fundamental insights for of a broad class of metal/ceramic interfaces degradation gained within this project allowed for the identification of critical interfacial debonding properties in complex interfacial systems (such as pellet-clad) operating in extreme environments (such as high burnup). Such studies have advanced the technical basis to assess the role of interfacial aging on the integrity of high burnup spent-fuel. The capabilities developed in this work allowed for preclusion of studying the actual irradiated fuel pellet-clad systems.

Overall this work provided answers to the following questions:

- **What microstructural features impact interfacial pellet-clad stability and debonding? And what is the impact of the environment (temperature, radiation conditions, loading) on interfacial inter-mixing and interfacial debonding?**
  - The fracture energy of $Ce_{1-x}Zr_xO_2(111)/CeO_2(111)$ increases markedly with Zr content. These findings suggest the **crucial role of Zr acting as a binder at the** $Ce_{1-x}Zr_xO_2/CeO_2$ **interfaces**, due to the more covalent character of Zr–O bonds compared to Ce–O.
  - Discrepancies between atomistic models and theoretical predictions of miscible interfaces that can be found in spent nuclear fuel pointed out the predominant role of the chemical binding over elastic interactions due to phase boundaries structures.
  - Investigations of spent fuel from H.B. Robinson Nuclear Generating Station and of monolithic U-10Mo fuel with Zr barrier layer interfaces show extremely complex high-burnup structures. Interface characterization highlighted key interface features including: ultrafine grain size refinement, precipitation of solid fission products, formation of intermetallic rich region and formation of a nanocrystalline porous.
- **Can we use surrogate interfaces integrated with associated computational model as a viable substitute to high burnup spent nuclear fuel system?**
  - Rastered ion irradiation led to complete deconstruction of the CeO_2 NP morphology, independent of the processing route or initial morphology, while maintaining the same

phase. This indicates that CeO_x under certain conditions is not a useful simulant for UO_2.

References

[1] Wesley Barrows, Rémi Dingreville, and Douglas Spearot. Traction–separation relationships for hydrogen induced grain boundary embrittlement in nickel via molecular dynamics simulations. *Mat. Sci. Eng. A-Struct.*, 650:354–364, 2016.

[2] S.J. Blair, B.R. Muntifering, R.O. Chan, C.M. Barr, T.J. Boyle, and K. Hattar. Unexpected radiation resistance of core/shell ceramic oxide nanoparticles. *Mater. Today Comm.*, 2018.

[3] T.J. Boyle, J.M. Sears, D. Perales, R.E. Cramer, P. Lu, R.O. Chan, and B.A. Hernandez-Sanchez. Synthesis and Characterization of Tris (trimethylsilyl) siloxide Derivatives of Early Transition Metal Alkoxides That Thermally Convert to Varied Ceramic–Silica Architecture Materials. *Inorg. Chem.*, 57(15):8806–8820, 2018.

[4] S. A. Briggs, T. J. Boyle, D. Perales, J. Kolar-Guitterez, J. M. Sears, D. T. Yonemoto, E. Sivonxay, and K. Hattar. Radiation stability of morphologically varied cerium oxide simulants. *in preparation*, 2018.

[5] D.C. Bufford, C.S. Snow, and K.M. Hattar. Cavity formation in Molybdenum studied in situ in TEM. *Fusion Sci. Technol.*, 71(3):268–274, 2017.

[6] E.Y. Chen, R. Dingreville, and C. Deo. Misfit dislocation networks in semi-coherent miscible phase boundaries: An example for U–Zr interfaces. *Comput. Mater. Sci.*, 154(3):194–203, 2018.

[7] J.-P. Crocombette, A. Chartier, and W.J. Weber. Atomistic simulation of amorphization thermokinetics in lanthanum pyrozirconate. *Applied Phys. Lett.*, 88(5):051912, 2006.

[8] C.A. Dennett, K.P. So, A. Kushima, D.L. Buller, K. Hattar, and M.P. Short. Detecting self-ion irradiation-induced void swelling in pure copper using transient grating spectroscopy. *Acta Mater.*, 145:496–503, 2018.

[9] R. Dingreville, D. Aksoy, and D.E. Spearot. A primer on selecting grain boundary sets for comparison of interfacial fracture properties in molecular dynamics simulations. *Sci. Rep.*, 7(1):8332, 2017.

[10] K. Edsinger, C.R. Stanek, and B.D. Wirth. Light water reactor fuel performance: Current status, challenges, and future high fidelity modeling. *JOM*, 63(8):49–52, 2011.

[11] P. A. Juan and R. Dingreville. Mechanics of finite cracks in dissimilar anisotropic elastic media considering interfacial elasticity. *J. Mech. Phys. Solids*, 99:1–18, 2017.

[12] P. A. Juan and R. Dingreville. Elastic Green's Function in Anisotropic Bimaterials Considering Interfacial Elasticity. *J. Elast.*, 131(2):277–296, 2018.

[13] N. Marchal, C. Campos, and C. Garnier. Finite element simulation of pellet-cladding interaction (PCI) in nuclear fuel rods. *Comp. Mater. Sci.*, 45(3):821–826, 2009.

[14] G. Martin, P. Garcia, C. Sabathier, L. Van Brutzel, B. Dorado, F. Garrido, and S. Maillard. Irradiation-induced heterogeneous nucleation in uranium dioxide. *Phys. Lett. A*, 374(30):3038–3041, 2010.

[15] P. McConnell, R. Wauneka, S. Saltzstein, and K. Sorenson. Normal Conditions of Transport Truck Test of a Surrogate Fuel Assembly. Technical Report M2-FCRD-UFD-2014-0000066, Fuel Cycle Research & Development. Used Fuel Disposition Campaign, 2014.

[16] Y. Miao, D. Aidhy, W.-Y. Chen, K. Mo, A. Oaks, D. Wolf, and J.F. Stubbins. The evolution mechanism of the dislocation loops in irradiated lanthanum doped cerium oxide. *J. Nucl. Mater.*, 445(1-3):209–217, 2014.

[17] G. Pastore, L. Luzzi, V. Di Marcello, and P. Van Uffelen. Physics-based modelling of fission gas swelling and release in UO_2 applied to integral fuel rod analysis. *Nucl. Eng. Design*, 256:75–86, 2013.

[18] Steve Plimpton. Fast parallel algorithms for short-range molecular dynamics. *J. Comput. Phys.*, 117(1):1–19, 1995.

[19] D.E. Spearot, R. Dingreville, and C.J. O'Brien. Atomistic simulation techniques to model hydrogen segregation and hydrogen embrittlement in metallic materials. In C.-H. Hsueh, S. Schmauder, C.-S. Chen, K.K. Chawla, N. Chawla, W. Chen, and Y. Kagawa, editors, *Handbook of Mechanics of Materials*, chapter 10, pages 1–34. Springer Singapore, 2018.

[20] L. A. M. Steele, T. J. Boyle, R. A. Kemp, and C. Moore. The selective insertion of carbon dioxide into a lanthanide(iii) 2,6-di-t-butyl-phenoxide bond. *Polyhedron*, 42(1):258–264, 2012.

[21] A Stukowski, VV Bulatov, and A Arsenlis. Automated identification and indexing of dislocations in crystal interfaces. *Modelling and Simulation in Materials Science and Engineering*, 20(8):085007, 2012.

[22] C. Sun, D.J. Sprouster, K. Hattar, L.E. Ecker, L. He, Y. Gao, Y. Zhang, and J. Gan. Formation of tetragonal gas bubble superlattice in bulk molybdenum under helium ion implantation. *Scripta Mater.*, 149:26–30, 2018.

[23] C.A. Taylor, D.C. Bufford, B.R. Muntifering, D. Senor, M. Steckbeck, J. Davis, B. Doyle, D. Buller, and K.M. Hattar. In situ TEM multi-beam ion irradiation as a technique for elucidating synergistic radiation effects. *Mater.*, 10(10):1148, 2017.

[24] J.-A. Wang, H. Wang, and H. Jiang. FY14 Status Report: CIRFT Testing Results on High Burnup UNF. Technical Report M3-FCRD-UFD-2014-000314, ORNL/TM-2014/310, Fuel Cycle Research & Development. Used Fuel Disposition Campaign, 2014.

[25] P. F. Weck, P. A. Juan, R. Dingreville, and E. Kim. Density Functional Analysis of Fluorite-Structured $(Ce,Zr)O_2/CeO_2$ Interfaces. *J. Phys. Chem. C*, 121(27):14678–14687, 2017.

[26] P. F. Weck and E. Kim. Assessing Hubbard-Corrected AM05+U and PBEsol+U Density Functionals for Strongly Correlated Oxides CeO_2 and Ce_2O_3. *Phys. Chem. Chem. Phys.*, 18(38):26816–26826, 2016.

[27] P. Zarnas, R. Dingreville, and J. Qu. Mechanics of point defect diffusion near dislocations and grain boundaries: A chemomechanical framework. *Comput. Mater. Sci.*, 144:99–112, 2018.

DISTRIBUTION:

1 Samuel Briggs (Samuel.Briggs@oregonstate.edu)

1 MS 1056 C. Barr, 1884
1 MS 01349 Timothy J. Boyle, 1815
1 MS 1056 Khalid M. Hattar, 1882
1 MS 01315 Pierre-Alexandre Juan, 1881
1 MS 0747 Patrick Mattie, 8853
1 MS 1056 A. Monterrosa, 1884
1 MS 0779 Sylvia Saltzstein, 8845
1 MS 1315 Ryan Wixom, 1881
1 MS 0779 Philippe F. Weck, 8845
1 MS 0359 D. Chavez, LDRD Office, 1911
1 MS 0161 Legal Intellectual Property, 11500
1 MS 0899 Technical Library, 9536 (electronic copy)


Sandia National Laboratories